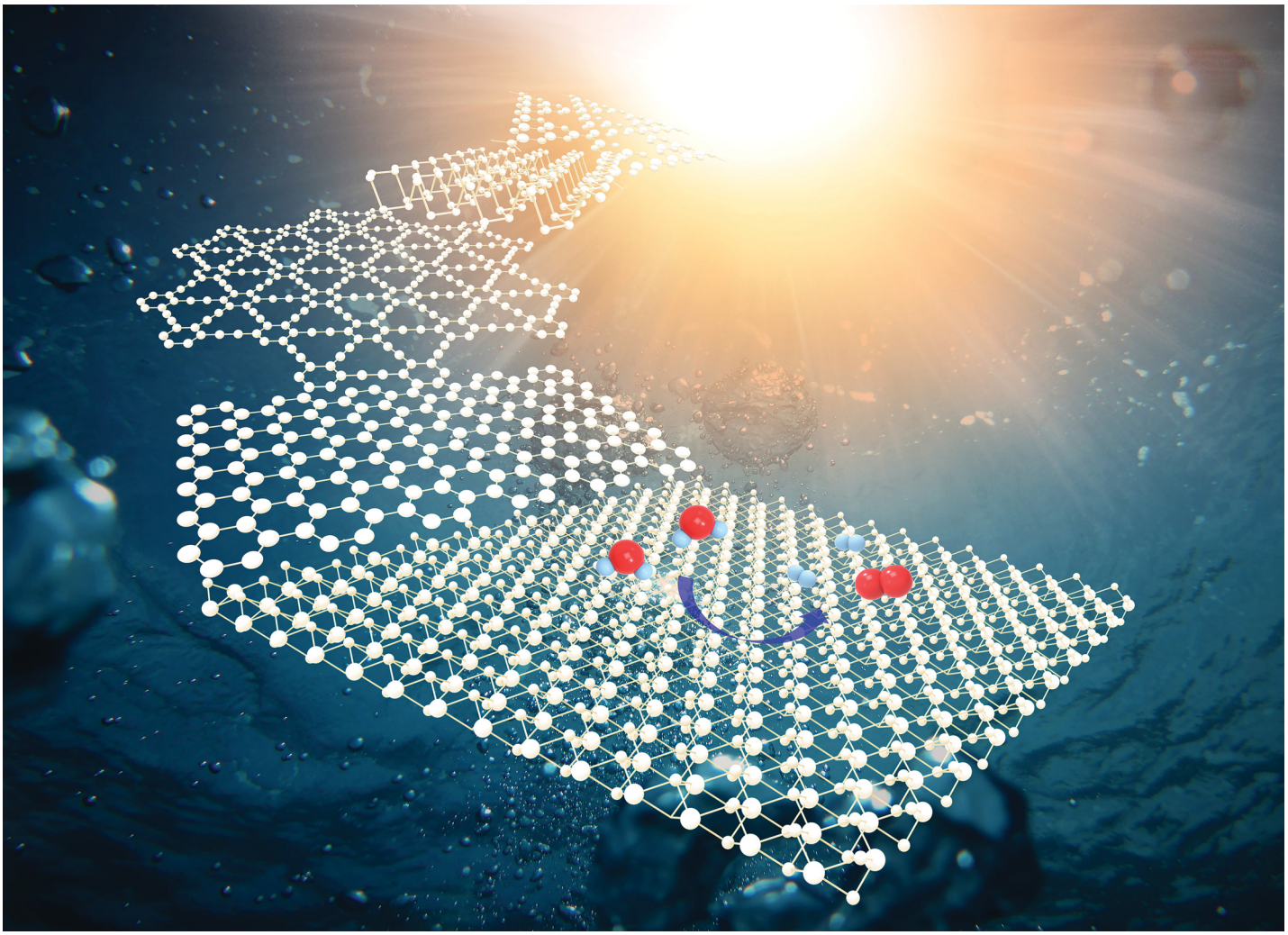

Showcasing research from Professor Jang's laboratory, Department of Materials Science and Engineering, Seoul National University, Seoul 08826, Republic of Korea.

Two-dimensional materials for photoelectrochemical water splitting

Two-dimensional materials (g-C_3N_4, black phosphorus, graphdiyne, graphene, and transition metal dichalcogenides) can serve as the bridge connecting the solar energy and sea water to accoplish the unbiased solar water splitting. Photons descend on a bridge consisting of two-dimensional materials and are replaced by electrons. Then, they participate in the reaction in which two water molecules are split into two hydrogen and one oxygen molecules.

As featured in:

See Ho Won Jang *et al.*, *Energy Adv.*, 2023, **2**, 34.

ROYAL SOCIETY OF CHEMISTRY

rsc.li/energy-advances

Registered charity number: 207890

Energy Advances

ROYAL SOCIETY OF CHEMISTRY

REVIEW ARTICLE

View Article Online
View Journal | View Issue

Cite this: *Energy Adv.*, 2023, 2, 34

Two-dimensional materials for photoelectrochemical water splitting

Sang Eon Jun, †[a] Jae Kwan Lee†[a] and Ho Won Jang *[ab]

Two-dimensional (2D) materials have sparked in-depth research in various fields due to their entirely distinct electronic and mechanical properties compared to their bulk counterpart. In a photoelectrochemical cell, 2D materials can serve crucial roles by incorporating their unique and extraordinary characteristics into semiconducting photoabsorbers to boost the unassisted solar water splitting. To this end, this review summarizes the intrinsic superiorities of 2D materials derived using van der Waals interactions between individual layers and presents the utilization of 2D materials to improve the photoelectrochemical performance of photoelectrodes. In addition, the emerging state-of-the-art 2D materials, including transition metal dichalcogenides (TMDs), graphene, graphdiyne, black phosphorus (BP), layered double hydroxides (LDHs), g-C_3N_4, and MXenes, will be introduced. Delicately constructed heterostructures with photoabsorbers and 2D materials are capable of highly efficient light harvesting for both hydrogen and oxygen evolution. Finally, critical outlooks on developing synthetic technology for mass production, improving stability issues, and constructing tandem architectures for unbiased solar water splitting will be discussed.

Received 28th August 2022,
Accepted 26th October 2022

DOI: 10.1039/d2ya00231k

rsc.li/energy-advances

1. Introduction

Environmental pollution and the energy crisis on the earth are two of the most serious issues that must be addressed. To this end, renewable energy, including solar and wind energy, have tremendous potential to alleviate the present sense of crisis due to its abundance.[1] Especially, the amount of solar energy radiated on the earth in 1 hour is similar to all of the energy consumed on the earth in a year.[2] To convert sunlight into useful electricity, various types of photovoltaic cells have been invented and they are now being operated in our daily life. However, high variability and intermittency of sunlight illumination could degrade the stability of the electrical grid when an enormous amount of electricity is generated instantly.[3]

[a] *Department of Materials Science and Engineering, Research Institute of Advanced Materials, Seoul National University, Seoul 08826, Korea. E-mail: hwjang@snu.ac.kr*
[b] *Advanced Institute of Convergence Technology, Seoul National University, Suwon, 16229, Republic of Korea*
† These authors contributed equally to this work.

Sang Eon Jun

Sang Eon Jun is currently a PhD candidate under the supervision of Prof. Ho Won Jang in the Department of Materials Science and Engineering at Seoul National University (SNU). He received his BS degree from the School of Integrative Engineering, Chung-Ang University, in 2019. His research focuses on the synthesis and characterization of 2-dimensional materials and single atom catalysts for energy conversion applications.

Jae Kwan Lee

Jae Kwan Lee is currently a PhD candidate under the supervision of Prof. Ho Won Jang in the Department of Materials Science and Engineering of Seoul National University (SNU). He received his BS degree from the Advanced Materials Science and Engineering, Sungkyunkwan University, in 2022. His current research focuses on the structure/morphology control of transition metal-based hydroxide via electrodeposition and its application to electrochemical water splitting.

In addition, it is difficult to transmit intensively produced electricity from one area to another area where the electrical grid is not connected. As a result, it is necessary to construct an energy storage system suitable for stable production, distribution, and utilization.[4–6] Compared to electricity, hydrogen can be stored independently without any network and it is easy to transport by land and sea for worldwide distribution.[7,8] Furthermore, it is expected to become sustainable future energy due to its non-toxicity, zero-emission, and large energy density.[9] It can be obtained by an electrochemical approach integrated with solar harvesting systems such as photovoltaic–electrochemical (PV–EC) and photoelectrochemical (PEC) water splitting.[10–12] In the PV–EC system, the electricity generated from a photovoltaic cell is supplied to an electrochemical water electrolyzer and converts H_2O into H_2 and O_2 while the photogenerated charges participate in hydrogen and oxygen evolution reaction at the surface of photoelectrodes in the PEC system.[13] Compared to PEC, the advantage of PV–EC is that the matured technologies are developed in both solar cells and water electrolyzers. Also, the solar-to-hydrogen efficiency of PV–EC is higher than that of PEC until now. However, for practical solar hydrogen production exhibiting both high efficiency and low system complexity, it is necessary to develop PEC cells with efficiency greater than 10% and stability of more than 10 years.[14] To meet these criteria, various types of semiconducting materials have been investigated for photoelectrochemical light harvesting.[13–15] For photocathodes where photoinduced hydrogen evolution reaction (HER) occurs, p-type semiconductors such as p-Si,[16] Cu_2O,[17] Sb_2Se_3,[18] and CIGS[19] have been widely studied. In the case of photoanodes in which photo-assisted oxygen evolution reaction (OER) occurs, n-type semiconductors including n-Si,[20–23] TiO_2,[24–26] WO_3,[27] $BiVO_4$,[28,29] and α-Fe_2O_3[30] have been reported. Although these materials have the potential to be utilized as photoelectrodes for unassisted solar water splitting,[31] there are still limitations to obtaining enough solar-to-hydrogen (STH) efficiency and stability to fulfill cost-effective hydrogen production.[32,33] It is derived from various factors such as insufficient output photovoltage, catalytic inactivity, light reflection on the surface, and photo/chemical-induced corrosion of photoelectrodes.[12,34,35] Hence, it is crucial that the photoelectrodes be assisted by the PEC catalysts. Also, the appropriate atomic-scale designs including engineering of defect, heteroatom, facet, phase, and single atoms are needed for both the photoelectrodes and catalysts to facilitate the photogenerated charge transfer and surface catalytic reaction.[36]

Two-dimensional (2D) materials have been extensively investigated for PEC catalysts with exceptional properties which could replace noble metals (Pt, IrO_x, and RuO_x).[37,38] They have recently emerged as promising materials in energy harvesting, storage, and conversion because of their large specific surface area,[39] stackability for heterostructure construction,[40] surface functionalization,[41] and thickness-dependent optoelectronic properties.[42] With these properties, they serve crucial roles as active PEC catalysts, interfacial transporting layers, passivation layers, and light harvesters for both HER and OER. Specifically, 2D materials with edge sites, defects, phase transformation, ion-exchanged sites, and synergistic composites can dramatically lower the free energy required for the surface reaction. Also, they become the charge transport mediators by being junctioned (Schottky junction, p–n junction, and multi-heterojunction) with semiconducting photoelectrodes. In addition, the surface of photoelectrodes vulnerable to the electrolyte is protected by electrochemically stable 2D materials and it leads to long-term stability. 2D materials having band gap even can be used for photon harvesters and their PEC performance can be improved by surface treatments and heterostructures.

In this review, we focus on 2D materials and their properties to acquire a significantly efficient and stable photoelectrode. Fig. 1 shows the representative 2D materials and their roles in photoelectrochemical water splitting. Firstly, the unique characteristics and superiorities of 2D materials will be introduced. Secondly, we review how 2D materials have been utilized for PEC water splitting and their roles in active catalysts, interfacial transporting layers, passivation layers, and light harvesters. Thirdly, the state-of-the-art 2D materials including transition metal dichalcogenides (TMDs), noble metal dichalcogenides, graphene, graphdiyne, black phosphorus (BP), layered double hydroxide (LDHs), g-C_3N_4, and MXenes will be introduced. Finally, several insights regarding the synthetic approach for mass production, stability issues derived from the desorption of 2D materials, and tandem devices for unassisted solar water splitting will be discussed with a perspective on future challenges and suggest solutions to enhance the photoelectrochemical performance.

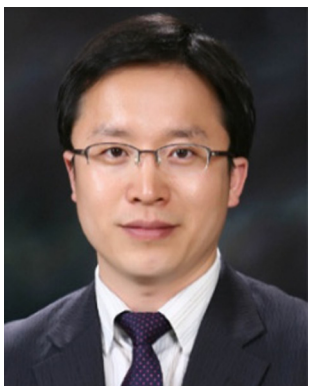

Ho Won Jang

Ho Won Jang is a full professor at the Department of Materials Science and Engineering in Seoul National University. He received his PhD from the Department of Materials Science and Engineering at Pohang University of Science and Technology in 2004. He worked as a research associate at the University of Madison-Wisconsin from 2006 to 2009. Before he joined Seoul National University in 2012, he worked at the Korea Institute of Science and Technology (KIST) as a senior research scientist. His research interests include materials synthesis and device fabrication for (photo)electrocatalysis, chemical sensors, memristors, micro-LEDs, and thin film transistors.

2. Superiority of 2D materials

The layers of 2D materials interact with each other *via* weak van der Waals force, while strong covalent bonds exist within

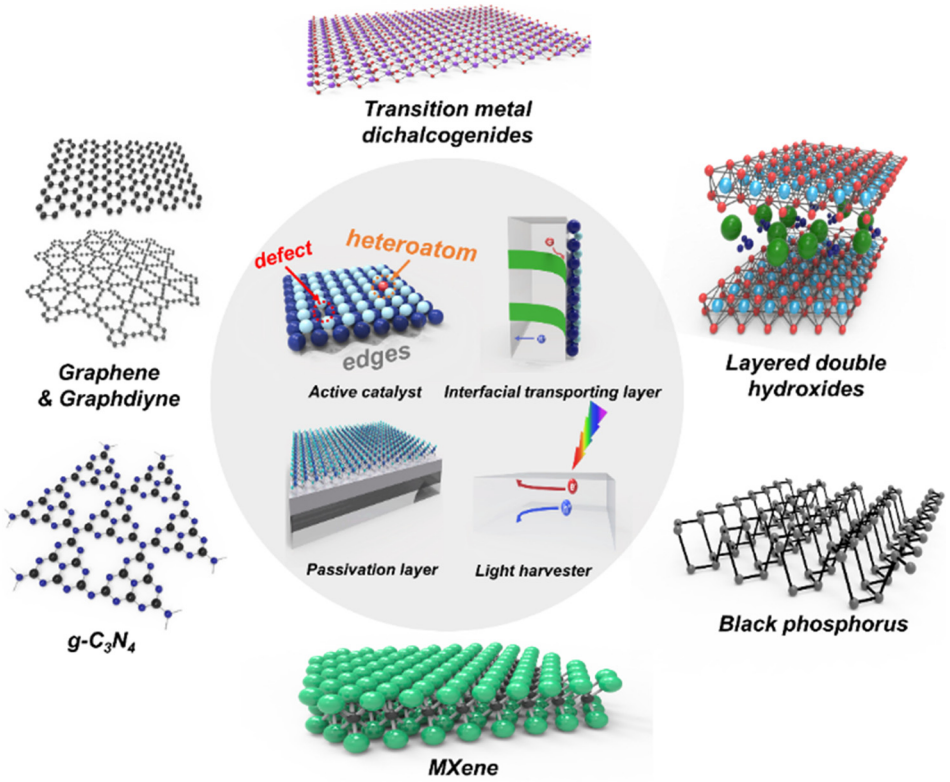

Fig. 1 Schematic illustrations of 2D materials and their roles in photoelectrochemical water splitting.

the plane.[43,44] Using weak interlayer interactions, it is possible to exfoliate 2D materials into monolayers or nanosheets. These interactions, the most remarkable characteristic of 2D materials, provide the unique superiorities that a material with 0D, 1D, and 3D network structure can not possess such as large specific surface area,[45] stackability for heterostructure,[37] bandgap tuning,[46] and surface functionalization.[47]

2.1. Large specific surface area

The large lateral size with ultrathin thickness enables 2D materials to have a high specific surface area. It allows the maximized active planes and atoms to be exposed. Hence, 2D materials are versatile for surface-active applications, including energy conversions, batteries, supercapacitors, gas sensors, *etc.* in which the reactants interact at the surface. For energy conversion applications such as HER, OER, and CO2RR, a large number of active sites where the reacting elements (H^+, OH^-, and CO_2) participate in the reaction are provided.[48] The larger the specific surface area, the more efficiently the reactants are consumed, and a larger amount of desired resultants are obtained. For various types of batteries using Li^+, Na^+, and Zn^+ as transporting ions, the improved ion absorption and transportation are achieved by large surface area and shortened transfer path, respectively, leading to high energy density and rate capability.[49] In terms of gas sensing applications, a large surface area of 2D materials provides numerous active sites for gas adsorption resulting in a strong improvement in the sensitivity of the sensor.[50]

2.2. Stackability for heterostructure

The van der Waals interactions enable 2D materials to be stacked into arbitrary substrates or layers without crystal mismatch and atomic interdiffusion, while conventional covalently bonded materials mechanically affect adjacent layers.[37] Especially, atomic scale high-quality heterostructures are realized by stacking different 2D materials on top of each other.[44] The most intriguing aspect is that high-quality Schottky junctions, p–n junctions, and multi-heterojunctions are achieved without intrinsic surface states within the energy band gap of 2D materials. It reduces the possibility of charge recombination, achieving a longer lifetime of charges going through the heterointerface. In addition, the local electron density of 2D heterostructures can be redistributed *via* van der Waals forces, leading to unpaired orbital electrons derived from a change in electron configuration.[51] This phenomenon induces easier molecule adsorption and desorption, boosting the surface catalytic reaction. For these reasons, they provide flexibility to be utilized with lots of van der Waals heterostructure combinations (0D–2D, 1D–2D, 2D–2D, and 3D–2D).[52] These combined dimensionality offer possibilities in various applications including energy conversions and storages,[53,54] optoelectronics,[55] sensors,[56] and field-effect transistors.[57]

2.3. Tunable band gap

The energy band gap implies the minimum energy demanded to excite an electron from the valence energy band (ground state) into the conduction energy band.[58] In van der Waals

layered structures, the band gap can be controlled by the number of layers due to the electron confinement along horizontal sheets and the energy splitting of band edges derived from the interlayer hopping.[59] There are several 2D materials having adjustable energy band gaps ranging from the mid-infrared in BP, visible in TMDs, to the ultraviolet in h-BN. Not only the thickness, many studies have revealed that the band gaps of 2D materials can be tuned by heterostructuring,[60] strain engineering,[61] intercalations,[62] chemical doping,[63] and alloying.[64] For instance, when a large strain is applied to the graphene, the inversion symmetry of the crystal lattice is broken, enabling it to open a bandgap in its gapless band structure.[65,66] Also, $Mo_{1-x}W_xS_2$ monolayer, one of the TMD alloys, shows the band gap bowing depending on W composition.[67] It is attributed to the unequal contribution of metal elements to the lowest unoccupied molecular orbital (LUMO) of the alloy, resulting in the occurrence of LUMO bowing. These thickness, mechanical, and composition-dependent band gap emission of 2D materials play crucial roles in devices requiring optimal band alignment such as field effect transistors, light-emitting diodes, and photoelectrodes/photocatalysts.

2.4. Surface functionalization

The pristine state of 2D materials has a certain degree of innate active sites such as edges and defects. However, by enlarging these active sites or introducing foreign impurities on the surface, unique mechanical, electrical, magnetic, and electrochemical properties can be obtained. In particular, chemical doping and anchoring functional units onto 2D materials induce novel properties improving dispersibility, wettability, processability, and environmental stability.[47] There are two types of 2D material functionalization depending on the way of interactions, which are non-covalent and covalent conjugation. The non-covalent method controls the electronic and physical properties without distorting crystal structures and physically adsorbed elements cause an effect *via* van der Waals or electrostatic forces.[68] On the other hand, covalent modification induces the rehybridization of orbitals by constructing covalent chemical building blocks between 2D materials and reactive molecules.[69] Both of them utilize molecular building blocks which can ultimately change the electronic characteristics of 2D materials *via* charge transfer or dipole-dipole interactions.[70]

3. Utilization of 2D materials in PEC water splitting

3.1. Active catalysts

In a photoelectrochemical water splitting system, one of the most crucial roles of 2D materials is boosting the catalytic reaction at the surface by lowering Gibbs free energy of ion adsorption and gas desorption. Despite the high activity of noble metal catalysts (Pt, IrO_x, and RuO_x), low-cost 2D materials have the potential to surpass precious metal catalysts *via* proper engineering. 2D materials intrinsically have catalytic active sites such as edges and defects. However, it is necessary to augment and expose them as much as possible to achieve vigorous photoelectrolysis.[71,72] Lots of studies have revealed that exceptionally active edges and defects can be induced by strain engineering,[73] plasma treatment,[74] foreign elements doping,[75] and so on. Li *et al.* theoretically predicted and verified that elaborately strained and electrochemically generated sulfur vacancies in the basal plane of monolayer MoS_2 serve as highly active sites for hydrogen evolution reaction.[76,77] Moreover, the highly active photoelectrochemical catalysts can be acquired by deliberately inducing phase transformation, exchanging anion or cation of 2D materials, and combining them with other materials exhibiting a synergistic effect.

3.1.1. Edge sites. Atoms residing on the edge sites of 2D materials have an unsaturated coordination environment compared to the atoms existing in the basal plane, showing considerably catalytic activity in the electrochemical reaction.[78] Fan *et al.* fabricated a highly efficient and stable p-Si photocathode by coating vertically standing grasslike MoS_2 using magnetron sputtering.[79] The edge-rich morphology of the MoS_2 layer on Al_2O_3/n^+p-Si, which was confirmed by SEM and TEM analysis, can enhance the catalytic activity for boosting hydrogen evolution reaction. Also, the MoS_2 layer exerts synergistic effects with the Al_2O_3 passivation layer to protect the surface of Si. These synergistic effects endow $MoS_2/Al_2O_3/n^+$p-Si photocathode to possess remarkable performance of onset potential (0.4 V *vs.* RHE), saturated photocurrent density (35.6 mA cm^{-2}), and stability (120 h). Jun *et al.* demonstrated the high-performance photocathode operating in the alkaline electrolyte by utilizing the hydrothermally grown MoS_2 nanoplates catalyst.[80] They were anchored on TiO_2 nanorods/p-Si photocathode exposing catalytically active edge sites. The high-resolution transmission electron microscopy (HR-TEM) image in Fig. 2(a) shows the lattice of layered MoS_2 nanoplates and the heterostructure interface. The lattice spacing is 0.617 nm, which corresponds to the (002) plane of MoS_2 and the edge sites are clearly observed. The purpose of designing edge-rich MoS_2 on the photocathode is demonstrated in Fig. 2(b). The edge of MoS_2 shows low hydrogen adsorption Gibbs free energy compared to inert basal planes, implying highly favorable proton adsorption and hydrogen desorption in acidic electrolyte. In alkaline media, they also enable the facile water dissociation in the Volmer reaction, accelerating alkaline hydrogen evolution. The photoelectrochemical catalytic effect of MoS_2 nanoplates in alkaline media was confirmed by comparing them with MoS_2 film in Fig. 2(c). The MoS_2 nanoplates/TiO_2 nanorods/p-Si showed dramatically enhanced PEC performance with an onset potential of 0.18 V *vs.* RHE and a photocurrent density of 10 mA cm^{-2} at 0 V *vs.* RHE.

3.1.2. Defects. Hill *et al.* revealed the photoelectrochemical catalytic effect of defects within p-type WSe_2 nanosheets by utilizing scanning electrochemical cell microscopy (SECCM) as a multifunctional tool.[81] Mechanically exfoliated p-WSe_2 on ITO substrate was anodized *via* hopping mode of SECCM and the hole-like defects were formed, revealed by atomic force microscopy (AFM). A photocurrent map and LSV curves of the defect array in Fig. 2(d) and (e) exhibit local variations of

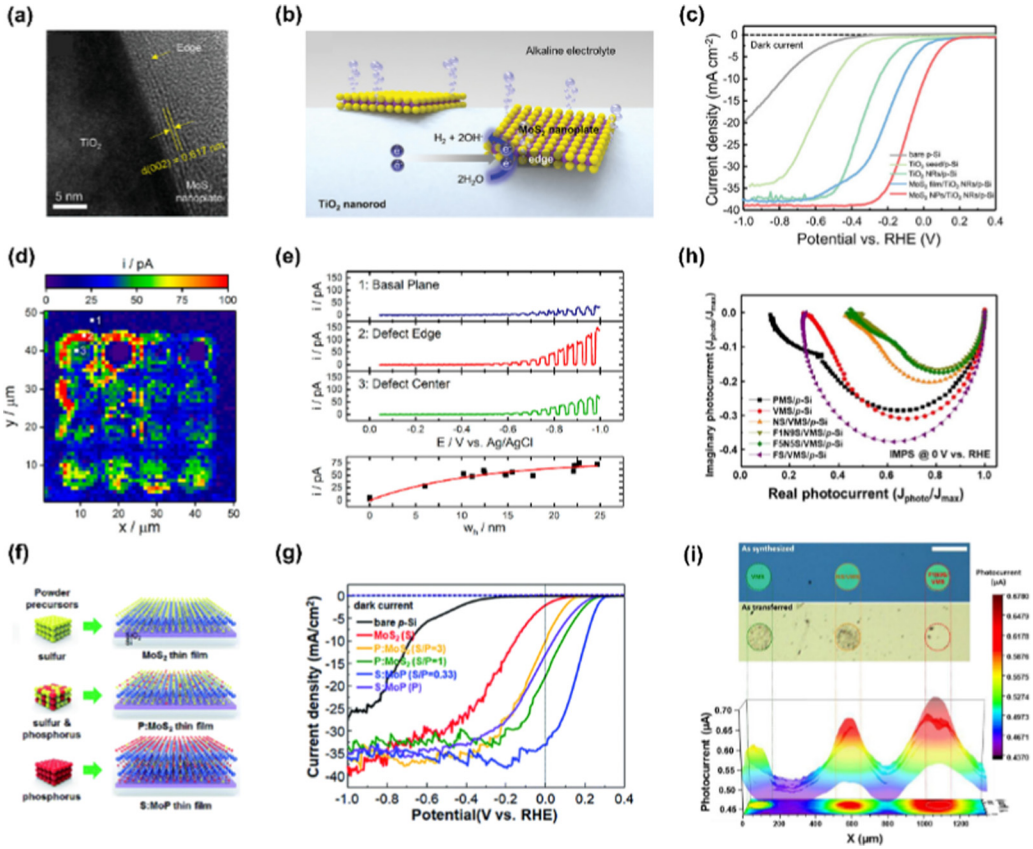

Fig. 2 (a) High-resolution TEM image of MoS_2 nanoplate having catalytically active edge sites decorated on TiO_2 nanorod. (b) Schematic illustration of MoS_2 nanoplates with large amounts of edges favorable for alkaline hydrogen evolution. (c) LSV curves of bare p-Si, TiO_2 seed/p-Si, TiO_2 nanorods/p-Si, MoS_2 film/TiO_2 nanorods/p-Si, and MoS_2 nanoplates/TiO_2 nanorods/p-Si photocathodes in 1 M KOH electrolyte. Copyright 2021, Wiley-VCH GmbH. (d) SECCM image with 1 μm resolution describing HER photocurrents of p-WSe_2 at −0.96 V *vs.* Ag/AgCl across the array of anodization defects. (e) *I*–*V* curves at basal plane, defect edge, and defect center in the SECCM image. Copyright 2020, American Chemical Society. (f) The photographic images of MoS_2, phosphorus-doped MoS_2, and sulfur-doped MoP thin film. (g) LSV curves of p-Si photocathodes with thin-film MoS_2, P:MoS_2, and S:MoS_2 catalysts. Copyright 2017, Royal Society of Chemistry. (h) IMPS Nyquist plot displaying the imaginary photocurrent *vs.* the normalized real photocurrent at 0 V *vs.* RHE. (i) Photocurrent mapping image of VMS, NS/VMS, and F1N9S/VMS catalysts. Copyright 2021, Elsevier.

photoelectrochemical HER activity. Compared to the unmodified-basal plane of WSe_2, the anodization defects (center and edge) exhibited a much higher current density derived from the enhanced catalytic activity. In particular, the defect edges were the most active region due to the enhanced carrier transport and local kinetic rates. Huang *et al.* executed defect engineering in 2D ReS_2/Si photocathode *via* Ar ion beam bombardment to maximize the catalytic active sites.[82] The Ar ion beam etcher produced atomic vacancy defects on the basal plane of ReS_2 nanosheets. The introduced Re vacancies not only increase the exposed S dangling bonds but also induce the charge compensation of S atoms in Re–Re bonds. As a result, an improved photocurrent density of -18.5 mA cm^{-2} at 0 V *vs.* RHE was achieved in $ReSe_2$/Si with 30 s ion beam bombardment.

3.1.3. Phase transformation. Recent studies have revealed that TMDs can exist in four polymorphs, which are the distorted tetragonal phase (1T), hexagonal phases (1H and 2H), and rhombohedral phase (3R).[83] Among them, metallic 1T phase TMDs show higher catalytic activity compared to those with other phases.[84] Since the 1T phase is thermodynamically metastable, it can be obtained *via* elaborately controlled procedures such as chemical exfoliation using Li^+, Na^+, and K^+ intercalation and salt-assisted transformation.[85–87] Ding *et al.* reported highly efficient and robust p-Si photocathode by depositing chemically transformed metallic 1T-MoS_2.[88] After directly growing 2H-MoS_2 nanosheets on Si by CVD, they were converted to metallic 1T-MoS_2 by n-BuLi treatment. The phase transformation was clearly identified by Raman and XPS analysis. Compared to 2H-MoS_2/p-Si, 1T-MoS_2/p-Si exhibited a lowered onset potential and higher photocurrent density at 0 V *vs.* RHE. It was revealed that the small charge transfer resistances at the interfaces and slow carrier recombination dynamics were achieved by 1T-MoS_2 and contributed to highly efficient PEC-HER.

3.1.4. Anion & cation exchanged sites. Kwon *et al.* obtained anion-exchanged 2D materials by simple thermolysis of spin-coated $(NH_4)_2MoS_4$ solution in ethylene glycol.[89] The ratio of sulfur and phosphorus powder for thermolysis determined the partial structural transition from 2D (MoS_2) to 3D (MoP) atomic structure as can be seen in Fig. 2(f). The substitutional dopant

phosphorus atoms easily exist in sulfur sites as the lattice structure of MoS_2 is similar to that of MoP and the atomic radii of sulfur and phosphorus are almost the same. They revealed that the lowered value of ΔG_H ($\sim$0.05 eV) of the S:MoP thin film, derived from increased dangling bonds on the surface, contributed to the enhanced PEC-HER activity. In Fig. 2(g), S:MoP (S/P = 0.33) thin film on p-Si photocathode showed the highest photocurrent density (33.13 mA cm^{-2}) at 0 V *vs.* RHE among MoS_2, P:MoS_2 (S/P = 3), P:MoS_2 (S/P = 1), S:MoP (S/P = 0.33), and S:MoP (P) catalysts.

3.1.5. Synergistic composites. Choi *et al.* demonstrated a synergistic composite PEC catalyst *via* one-step sulfurization of Fe/Ni/Mo thin film deposited by electron beam evaporation.[90] For the resultant of the process, the vertically oriented MoS_2 thin film decorated with $FeNiS_x$ nanoparticles was acquired. The DFT calculations revealed that the edge site of MoS_2, Fe-doped Ni_3S_2, and the interface between MoS_2 and Fe-doped Ni_3S_2 have a significantly lowered ΔG_H, promoting proton reduction in HER. Fig. 2(h) exhibits Nyquist plots of intensity-modulated photocurrent spectroscopy (IMPS) for probing the periodic changes in the photocurrent in response to a sinusoidal intensity modulation of the incident light illumination.[91] From these data, charge transfer and charge recombination constant of PMS/p-Si, VMS/p-Si, NS/VMS/p-Si, F1N9S/VMS/p-Si, F5N5S/VMS/p-Si, and FS/VMS/p-Si photocathodes were calculated. Among the samples, F1N9S/VMS/p-Si showed almost the best photogenerated charge transfer and recombination due to the vertically aligned domains of VMS and the catalytic activity of F1N9S. In Fig. 2(i), they also conducted scanning photoelectrochemical microscopy (SPECM) to visualize the intensity of the photocurrent generated on each catalyst into 3D mapping. It was confirmed that F1N9S/VMS catalyst showed the highest spatial photocurrent density among all the samples. In addition, F1N9S/VMS/p-Si photocathode exhibited remarkable PEC performance with a photocurrent density of 25.44 mA cm^{-2} at 0 V *vs.* RHE.

3.2. Interfacial transporting layers

The photo-induced charge carriers generated from semiconductors tend to make recombination before arriving at the surface of photoelectrodes. To achieve highly efficient charge flow from the semiconductor to the electrolyte, it is necessary to construct interfacial transporting layers. The 2D materials, which can easily be adjusted in thickness and constructed anywhere, are suitable for interfacial transporting layers. The electronic properties including band gap and work function can be acquired by analyzing X-ray photoelectron spectroscopy (XPS) and ultraviolet photoelectron spectroscopy (UPS). Using these data, energy band diagram regarding the junction of semiconducting photoabsorber and 2D material can be demonstrated. If the Schottky junction, p–n junction, and multi-heterojunction are established at the interface, the photogenerated charges can easily transfer by the electric field derived from energy band bending. In addition, 2D materials are capable of inhibiting the formation of secondary compounds between photoelectrode and catalyst. As the interfacial secondary compound hinders the charge transport, it is necessary to prevent them by using 2D materials that can be stacked into substrates without crystal mismatch and atomic interdiffusion.

3.2.1. Schottky junction. Yang *et al.* introduced a novel charge transfer system by inserting 2D MXene nanosheets (MNs) between α-Fe_2O_3 and oxygen evolution catalysts (OECs).[92] The high hole mobility of MNs and the built-in electric field between MNs and α-Fe_2O_3 enable MNs to act as the charge transfer mediators to efficiently restrain the interfacial charge recombination. In Fig. 3(a), HR-TEM showed a distinct interfacial structure with ultrathin 2D MNs sticking to the α-Fe_2O_3. Using UPS, the energy band structures of MNs and α-Fe_2O_3 were investigated in Fig. 3(b). As the work function of MNs is larger than that of α-Fe_2O_3, the Schottky junction is established at the interface, leading to an upward energy band bending under illumination. As a result, the photogenerated holes easily transfer and separate to the electrolyte due to the built-in electric field. In Fig. 3(c), the chopped LSV curve of α-Fe_2O_3 photoanode with MNs interlayer and Co–Pi catalyst showed the highest photocurrent density (2.54 mA cm^{-2}) at 1.23 V *vs.* RHE. Ku *et al.* boosted the photoelectrochemical performance of 3D pyramid-like p-Si by constructing a Schottky junction between graphene and silicon.[93] Ethylene-vinyl acetate (EVA) was used to transfer graphene onto a 3D pyramidal Si and high-quality graphene was deposited. By utilizing localized electrochemical impedance spectroscopy (LEIS), relatively low impedance was shown in the graphene/p-Si interface, which indicates that fast charge transfer was accomplished at the interface between the graphene/Si Schottky junction and the electrolyte. As a result, the fabricated 3D pyramid-like graphene/p-Si photocathode with Pt catalyst exhibited a high photocurrent density of -32.5 mA cm^{-2} at 0 V *vs.* RHE.

3.2.2. p–n junction. Kwon *et al.* applied an n-type MoS_2 thin film into a p-type silicon photocathode to establish a p–n junction at the interface.[94] The UPS and XPS analysis were carried out to obtain an energy band diagram of the silicon photocathode and MoS_2 thin-film catalyst in Fig. 3(d). From the secondary electron emission (SEE) spectra, the work function of p-Si and MoS_2/p-Si were estimated as 4.7 and 4.5 eV, respectively. According to the XPS valence-band spectra, the energy difference between the Fermi level and the valence band maximum ($E_F - E_V$) of p-Si and MoS_2/p-Si were 0.4 and 1.4 eV, respectively. Based on these results, the energy band diagram of n-MoS_2/p-Si is provided in Fig. 3(e). It was confirmed that the transfer of photo-induced charges is energetically favorable without an electronic potential barrier. Ghosh *et al.* improved water splitting ability by combining 2D-MoS_2 with etched p-GaN [p-GaN(Et)].[95] The p–n junction was formed at the interface between p-type GaN and n-type MoS_2. The valence band maximum (VBM) of pristine p-GaN(Et) was located at 0.93 eV below the Fermi level (E_F) but that of p-GaN/MoS_2 was shifted to 0.28 eV below E_F. This shift caused more p-type nature, leading to more intense band bending at the interface. As a result, the formation of 2D MoS_2 layer on p-GaN(Et) enhanced the carrier transport efficiency. Moreover, this downward band bending efficiently decreases the recombination at the interface between electrode and electrolyte by hindering the

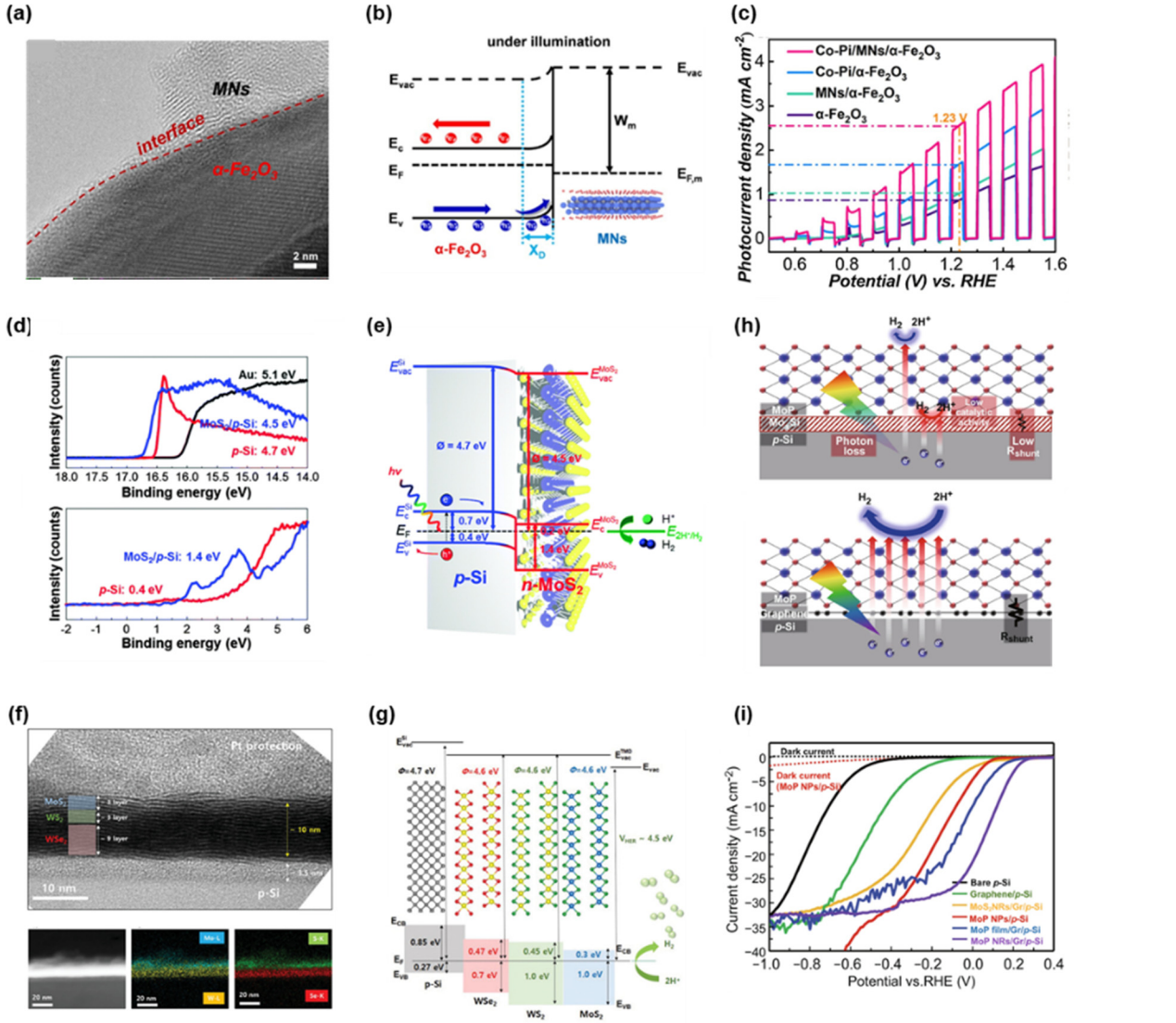

Fig. 3 (a) High-resolution TEM image of MXene nanosheets/α-Fe_2O_3. (b) Energy band diagram of MXene nanosheets/α-Fe_2O_3 Schottky junction under illumination. (c) LSV curves of α-Fe_2O_3, MNs/α-Fe_2O_3, Co–Pi/α-Fe_2O_3, and Co–Pi/MNs/α-Fe_2O_3. Copyright 2021, Elsevier. (d) UPS and XPS spectra of Au, p-Si, and MoS_2/p-Si. (e) Schematic of energy band diagram of the MoS_2/p-Si photocathode having p–n junction. Copyright 2016, Royal Society of Chemistry. (f) Cross-sectional high-resolution TEM image for 112-MWW′/p-Si thin film. (g) Schematic of energy band diagram of 112-MWW′/p-Si thin film. Copyright 2019, Wiley-VCH GmbH. (h) Schematic of MoP/Mo_xSi/p-Si and MoP/graphene/p-Si. (i) LSV curves of bare p-Si, graphene/p-Si, MoS_2 NRs/Gr/p-Si, MoP NPs/p-Si, MoP film/Gr/p-Si, and MoP NRs/Gr/p-Si. Copyright 2021, Springer Nature.

hole flow. Due to this effect, the p-GaN/MoS_2 photocathode showed an elevated photocurrent density of -2.15 mA cm^{-2} at 0 V *vs.* RHE and hydrogen evolution rate of 89.56 μmol h^{-1} at -0.3 V *vs.* RHE.

3.2.3. Multi-heterojunction. Seo *et al.* synthesized large-scale multi-heterojunction TMD thin films (MoS_2/WS_2/WSe_2) on a p-type silicon photocathode using pulsed laser deposition (PLD).[96] The cross-sectional high-resolution TEM image in Fig. 3(f) showed that the total thickness of the thin film was 10 nm and the numbers of layers were 3, 3, and 9 for MoS_2, WS_2, and WSe_2, respectively. To reveal the band structure of the photocathode, the work function, optical bandgap, and energy difference between the Fermi level and valence band maximum ($E_F - E_V$) were acquired by UPS, UV-vis spectroscopy, and XPS. In Fig. 3(g), a schematic of the energy band diagram for MoS_2/WS_2/WSe_2/p-Si is provided and it has a multistaggered gap facilitating the transfer of photogenerated electrons. The multi-TMD thin-film catalysts having multistaggered gaps enable the charges to transfer easily compared to homo-TMD thin-film catalysts.

3.2.4. Inhibition of compound formation. Jun *et al.* demonstrated 2D monolayer graphene as an interlayer between silicon photocathode and MoP nanorods catalyst to prevent the formation of a secondary compound (Mo_xSi) which absorbs a parasitic light and provides an inefficient electron path.[97] In Fig. 3(h), the schematics of photocathodes with MoP

catalysts synthesized on bare p-Si and graphene-passivated p-Si are shown. The inevitably formed Mo_xSi induces parasitic light absorption and it traps the photogenerated electrons due to the low shunt resistance, resulting in low catalytic activity in MoP catalysts. To solve this problem, the graphene interlayer was deposited on p-Si, leading to the inhibition of the secondary compound during the catalyst synthesis. As a result, the photo-induced electrons easily transfer to the surface of the MoP catalyst to participate in the hydrogen evolution reaction. In Fig. 3(i), MoP naoparticles/p-Si without graphene interlayer showed low PEC-HER performance and a discernible leakage current derived from a low shunt resistance of Mo_xSi. However, the MoP nanorods/graphene/p-Si photocathode showed a remarkable catalytic activity with a photocurrent density of 21.8 mA cm^{-2} at 0 V *vs.* RHE. It is attributed to the graphene interlayer suppressing the formation of silicide.

3.3. Passivation layers

Sim *et al.* introduced plasma-treated N-doped monolayer graphene on p-Si photocathode as both a PEC catalyst and a passivation layer.[98] To synthesize N-doped graphene, N_2-plasma with 10 W power was treated for 14 s. The passivation effect of graphene and N-doped graphene was investigated by 300 cycles of cyclic voltammetry (CV) in Fig. 4(a). As the CV cycle increased, bare Si showed a large negative shift. However, the silicon photocathodes with graphene and N-doped graphene exhibited only shifts in the onset potential of 0.1 and 0.035 V, respectively. In Fig. 4(b), XPS spectra of the Si 2p region for each sample before and after the stability test for 10 000 s were provided to reveal the capability of graphene to passivate the silicon surface. In the case of graphene and N-doped graphene on silicon, only a small increase in the Si–O peak was observed while the peak of bare Si increased a lot after the stability test. It indicates that graphene suppresses the oxidation of the silicon surface during photoelectrochemical hydrogen production.

King *et al.* demonstrated a stable silicon photocathode with a protecting layer that is composed of 2D molybdenum disulfide, molybdenum silicide, and silicon oxide.[99] In Fig. 4(c), the schematics of the MoS_2 catalyst and additional protection layers on the silicon photocathode are presented. They suggested two systems. One has two interlayers (Mo_xSi and Mo) and the other has three interlayers (SiO_2, Mo_xSi, and MoO_x). Fig. 4(d) shows the cross-sectional TEM image of a photocathode with three interlayers ($MoO_x/MoSi_x/SiO_2$) and it is concluded that the overall thickness of MoS_2 with three interlayers is greater than that of MoS_2 with two interlayers due to a thicker MoO_x and SiO_2. In Fig. 4(e), cyclic voltammograms of photocathode with three interlayers on both day 1 and day 62 showed an excellent onset potential of 0.31 V *vs.* RHE and photocurrent density, which proved the passivation effect of MoS_2 and three interlayers.

3.4. Light harvesters

Yu *et al.* investigated the role of defects on the PEC performance of 2D WSe_2 thin film photocathodes by applying two different treatments, a pre-exfoliation annealing and a post-

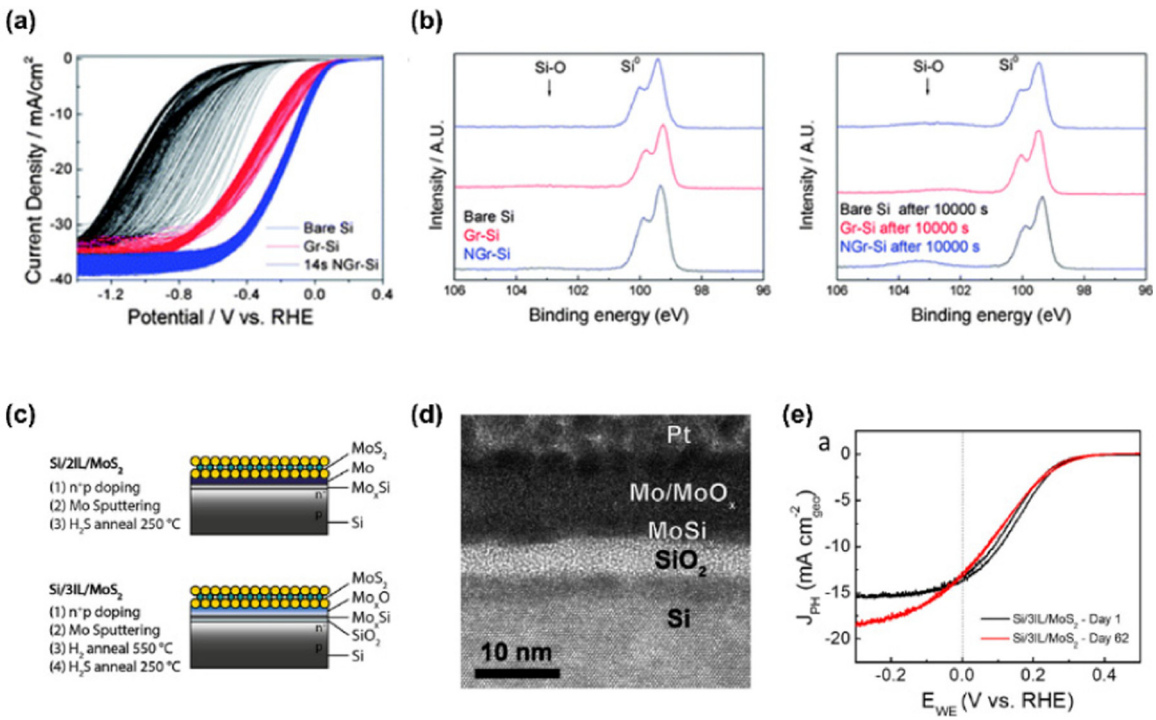

Fig. 4 (a) 300 cycles of CV test for bare Si, Gr-Si, and NGr-Si at pH 0. (b) XPS spectra of the Si 2p region for each sample before and after chronoamperometry test at 0 V *vs.* RHE for 10 000 s. Copyright 2013, Royal Society of Chemistry. (c) Schematics of MoS_2 catalyst and protection layers at the silicon interface. (d) TEM image of $MoS_2/Mo/MoO_x/Mo_xSi/SiO_2/Si$ photocathode. (e) Cyclic voltammograms of $Si/2IL/MoS_2$ on day 1 and 25. Copyright 2017, American Chemical Society.

deposition surfactant attachment to eliminate intraflake and edge defects, respectively.[100] The schematics of WSe_2 flake with treatments and the resulting atomic structures were provided in Fig. 5(a). After pre-exfoliation annealing, few internal Se vacancies exist at the lattice of WSe_2. In addition, the exposed edge vacancies were filled by surfactant after the treatment with hexyl-trichlorosilane. As can be seen in Fig. 5(b), the WSe_2 photocathode with both pre-exfoliation annealing and surfactant attachment showed the highest photocurrent density (4.0 mA cm^{-2}) at 0 V *vs.* RHE among the samples (Exfoliation with as-received WSe_2, HTS treatment after exfoliation with as-received WSe_2, exfoliation with pre-annealed WSe_2, and HTS treatment after exfoliation with pre-annealed WSe_2). While only the pre-annealing did not affect the performance, upon applying both the pre-annealing and HTS treatment, an enhanced PEC performance was identified.

Wang *et al.* analyzed charge recombination and transport pathways as a function of stacking configuration in MoS_2/WS_2 junction photoelectrode.[101] They performed the image analysis procedure to investigate parallel charge transport pathways. In Fig. 5(c), the optical transmission images and photocurrent maps of ITO/MoS_2/WS_2 and ITO/WS_2/MoS_2 are provided. The bright contrast pixels of MoS_2/WS_2 extended beyond the heterojunction boundary while the dark contrast pixels of WS_2/MoS_2 occur deeper within the heterojunction interior. To quantitatively analyze how the heterojunction influenced parallel charge transport, the photocurrent value *versus* distance between WS_2 and the nearest heterojunction edge site was obtained in Fig. 5(d). In the case of WS_2 on MoS_2, the photocurrent increased monotonically with decreasing *d* and showed a maximized value inside the heterojunction region. However, for the stacking configuration with WS_2 under MoS_2, the photocurrent decreased with decreasing *d*.

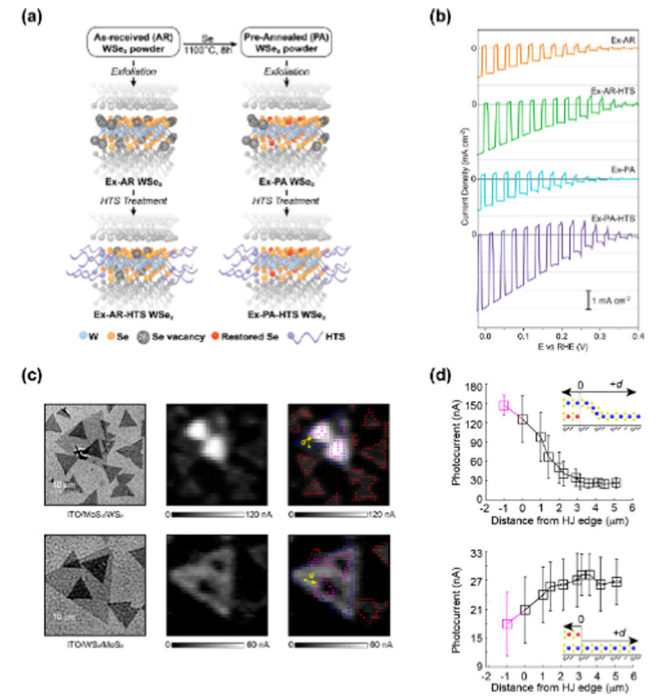

Fig. 5 (a) Schematic of the WSe_2 flake treatments and their proposed effect on defects. (b) LSV curves of Ex-AR, Ex-AR-HTS, Ex-PA, and Ex-PA-HTS WSe_2 nanoflake photoelectrodes. Copyright 2018, American Chemical Society. (c) Optical transmission images and photocurrent maps of ITO/MoS_2/WS_2 and ITO/WS_2/MoS_2. (d) Photocurrent of WS_2 and MoS_2 as a function of distance to the nearest heterojunction edge site. Copyright 2019, American Chemical Society.

4. State-of-the-art 2D materials for PEC water splitting

4.1. Transition metal dichalcogenides (TMDs)

TMDs are one of the most promising materials for PEC applications due to their unique optical, electrical, and catalytic properties. In particular, the edges and defects serve as good active sites, exhibiting excellent photoelectrochemical catalytic performance. Recently, various transition metal-based dichalcogenides consisting of MoS_2,[102] WS_2,[103] WSe_2,[96] NbS_2,[104] $PtSe_2$,[105] and $ReSe_2$[106] have been developed for solar water splitting with strategies such as edge engineering, morphology control, thickness control, and heterostructuring.

4.1.1. Non-noble metal-based TMDs. Andoshe *et al.* improved the photoelectrochemical catalytic performance of silicon photocathode by depositing 3D structured MoS_2 on TiO_2 coated p-Si substrate.[107] Fig. 6(a) shows a schematic illustration of 3D MoS_2/TiO_2/p-Si and a high-angle annular dark field-scanning TEM (HAADF-TEM) image of MoS_2. The deposited MoS_2 was grown into 3D structures with vertical, head-on collision, and defective bending, respectively. Their morphology was controlled by growth kinetics in metal-organic chemical vapor deposition (MOCVD). High precursor flow rates create sufficient nucleation sites, resulting in the formation of smaller grains and 3D structures. 3D MoS_2 shows the lowered optical reflectance and improved photoelectrochemical catalytic activity due to the 3D structure and exposed edge sites, respectively. The improved optical properties of 3D MoS_2 are shown in Fig. 6(b). Compared to TiO_2/p-Si, 3D MoS_2/TiO_2/p-Si has lower reflectance in all wavelength ranges. In Fig. 6(c), 3D MoS_2/TiO_2/p-Si shows enhanced HER performance with an onset potential of 0.35 V *vs.* RHE and a saturation current density of −37 mA cm^{-2}.

W-based TMDs also exhibit considerable photoelectrochemical catalytic properties. Hasani *et al.* conducted the direct synthesis of WS_2 on p-Si *via* the thermolysis process.[108] The surface of the silicon wafer has become hydrophilic by depositing the WO_3 layer as a pretreatment and $(NH_4)WS_4$ precursor was coated on a hydrophilic substrate with good adhesion. Then, the as-fabricated $(NH_4)WS_4/WO_3$/p-Si was converted to WS_2/p-Si by simple thermolysis at 900 °C. The thickness-optimized (38 nm) WS_2/p-Si photocathode showed great PEC performance with a photocurrent density of −9.8 mA cm^{-2} at 0 V *vs.* RHE and an onset potential of 0.022 V *vs.* RHE. In addition, the WS_2/p-Si photocathode showed good stability with no decrease in current density even after 40 h.

NbS_2 is a representative metallic TMDs having a highly active basal plane for hydrogen adsorption and desorption, as

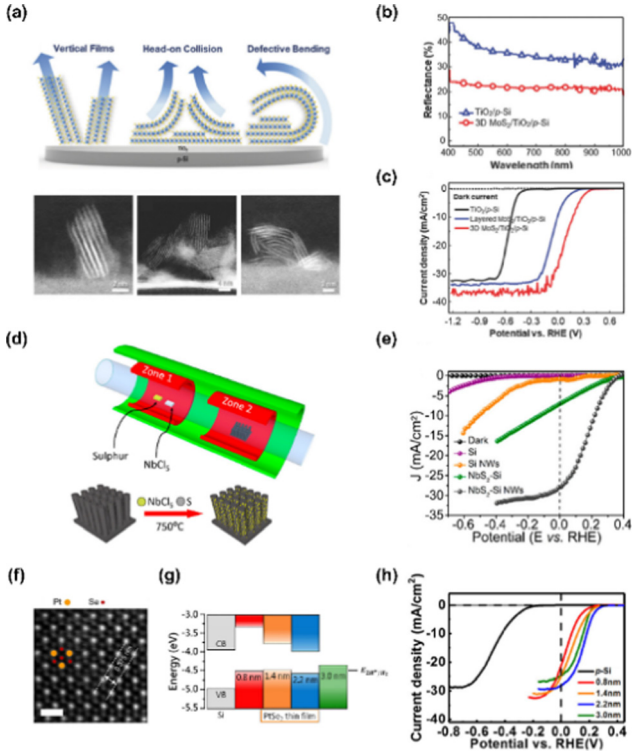

Fig. 6 (a) Schematic and HAADF-STEM images of vertically aligned 3D MoS_2 film at high precursor flux rate. (b) Reflectance spectra of TiO_2/p-Si and 3D MoS_2/TiO_2/p-Si at the incident angle of 40°. (c) LSV curves of TiO_2/p-Si, layered MoS_2/TiO_2/p-Si, and 3D MoS_2/TiO_2/p-Si. Copyright 2018, Wiley-VCH GmbH. (d) Schematic of NbS_2 growth on Si NWs using CVD method. (e) LSV curves of Si and NbS_2-deposited Si. Copyright 2019, American Chemical Society. (f) Annular-dark-field (ADF) scanning transmission electron microscopy (STEM) image of a $PtSe_2$ thin film. (g) Energy band diagram of p-Si and $PtSe_2$ thin films with the thickness of 0.8, 1.4, 2.2, and 3.0 nm. (h) LSV curves of p-Si photocathodes with 0.8, 1.4, 2.2, and 3.0 nm $PtSe_2$ catalysts. Copyright 2021, American Chemical Society.

can be identified by its near-zero hydrogen adsorption Gibbs free energy.[109] Gnanasekar *et al.* demonstrated an efficient and stable Si nanowires photocathode by depositing NbS_2 using a CVD method.[104] Fig. 6(d) shows the schematic image of NbS_2 growth on Si NWs using a CVD method. The LSV curves of the fabricated photocathodes are shown in Fig. 6(e) and NbS_2/Si NWs shows an onset potential of 0.34 V *vs.* RHE and photocurrent density of -28 mA cm^{-2} at 0 V *vs.* RHE.

4.1.2. Noble metal-based TMDs. Chung *et al.* synthesized 2D layered $PtSe_2$ on p-type Si photocathode by using a CVD method.[105] As the thickness of $PtSe_2$ decreases from bulk to monolayer, the properties change from semimetal to semiconductor. In addition, the improved electrical conductivity of $PtSe_2$ through thickness control contributes to the transfer of photogenerated charges. The annular-dark-field (ADF) scanning transmission electron microscopy image of the as-synthesized $PtSe_2$ thin film is presented in Fig. 6(f). From this image, it was identified that six Se atoms surrounded one Pt atom which is theoretically the most stable AA stacked 1T phase octahedral structure. Band diagrams of $PtSe_2$ thin films with different thicknesses are shown in Fig. 6(g). $PtSe_2$ films with thicknesses of 0.8, 1.4, and 2.2 nm exhibit p-type semiconductor behaviors and a thin film with a thickness of 3.0 nm exhibits a semimetallic behavior with a workfunction value of zero. As the thickness of the thin film increases, the energy level of the conduction band decreases, and the energy barrier at the $PtSe_2$/p-Si interface decreases. Therefore, the 2.2 nm $PtSe_2$ thin film has the most optimized band structure. The improved PEC performance by controlling the thickness of the $PtSe_2$ thin film is shown in Fig. 6(h). The 2.2 nm $PtSe_2$/p-Si photocathode exhibits the best PEC performance with an onset potential of 0.27 V *vs.* RHE and photocurrent density of -28.1 mA cm^{-2} at 0 V *vs.* RHE.

4.2. Carbon allotropes

4.2.1. Graphene. Graphene, a single-atom-thick carbon sheet having sp^2-hybridization, is an origin of intrinsically layered 2D materials and has attracted lots of attention mainly due to excellent chemical and physical properties such as strong ambipolar electric field effect,[110] unconventional quantum Hall effect,[111] high thermal conductivity,[112] high transparency,[113] high carrier mobility,[114] and mechanical strength,[115] *etc.*[116] Until now, graphene has been widely utilized in numerous research and it is also applicable to photoelectrochemical system as a catalyst,[117] charge mediator,[118] photon trapping layer,[119] morphology controller,[120] and interfacial transporting layer.[97] Sim *et al.* introduced high-transmittance graphene onto a silicon photocathode to enhance photon-to-current efficiency *via* layer control of graphene.[121] From the UPS measurement, it was revealed that double-layer graphene shows the smallest work function, indicating the conduction band edge is strongly bent to the H^+/H_2 redox couple. Consequently, the largest anodic shift in the LSV curve was achieved due to the strongest band bending in the depletion region. After plasma treatment for introducing large amounts of defects and edges, double-layer graphene/p-Si photocathode showed enhanced PEC performance with an efficiency of 0.32%, which is 64 times higher than that of bare p-Si.

4.2.2. Graphene oxide. Ning *et al.* fabricated a photoanode with highly enhanced PEC performance by synthesizing reduced graphite oxide (rGO) and NiFe-layered double hydroxide (LDH) on a TiO_2 nanorod array (NA).[122] In Fig. 7(a) and (b), SEM images of pristine TiO_2/NiFe-LDH NAs and TiO_2/rGO/NiFe-LDH NAs are shown, respectively and we can see that a larger lateral size of NiFe-LDH can be observed when rGO interlayer was applied. The rGO contributed to the increased electrical conductivity, facilitating the growth of NiFe-LDH. Fig. 7(c) schematically shows the PEC-OER process of TiO_2/rGO/NiFe-LDH NAs. It was revealed that the photogenerated electrons and holes from TiO_2 respectively transferred to rGO and NiFe-LDH due to the energy difference of the CBM between TiO_2 and rGO, and that of VBM between TiO_2 and NiFe-LDH. The migrated electrons propagate rapidly to the current collector due to the outstanding electron mobility of rGO, which remarkably improves the charge separation efficiency while holes captured in NiFe-LDH participate in OER. In Fig. 7(d), TiO_2/rGO/NiFe-LDH NAs showed an improved photocurrent

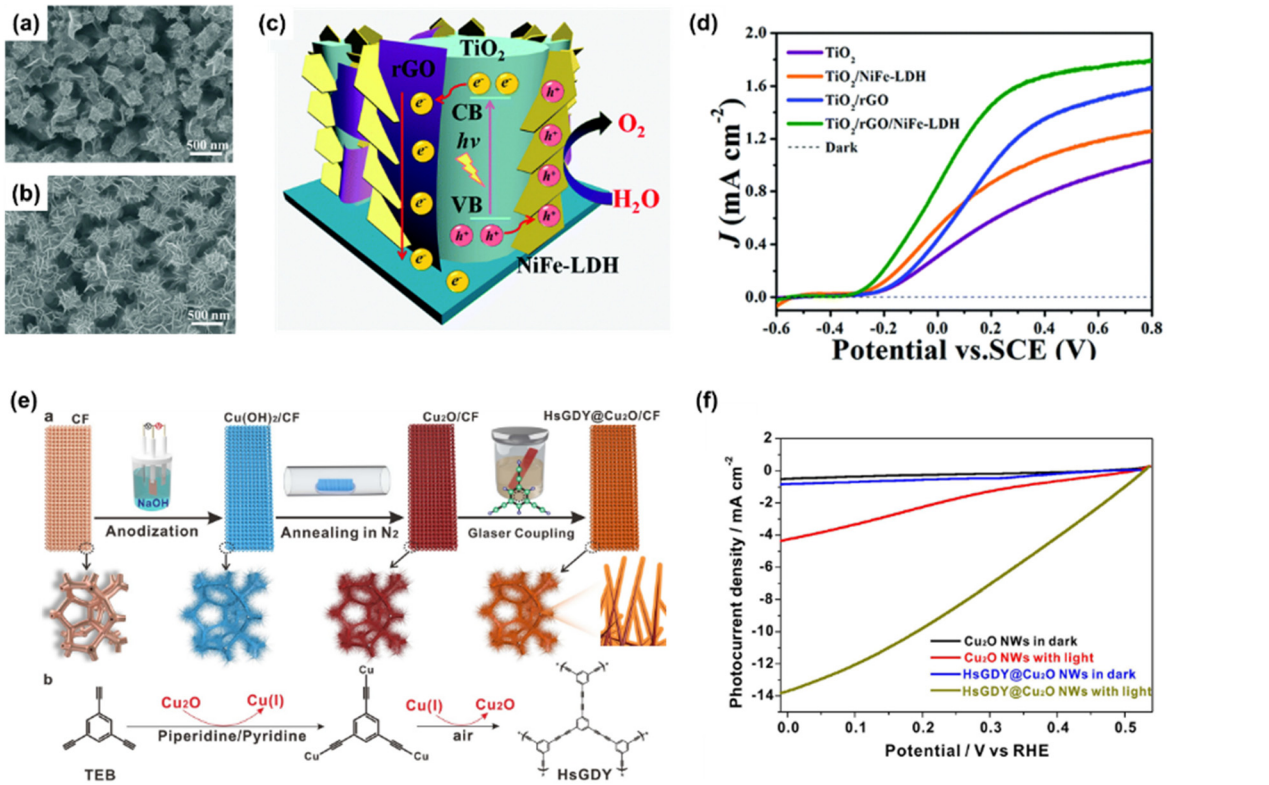

Fig. 7 SEM images of (a) TiO_2/NiFe-LDH NAs and (b) TiO_2/rGO/NiFe-LDH NAs. (c) Schematic of the PEC water oxidation process in the TiO_2/rGO/NiFe-LDH core–shell NA photoanode. (d) LSV curves of TiO_2, TiO_2/NiFe-LDH, TiO_2/rGO, and TiO_2/rGO/NiFe-LDH NAs. Copyright 2016, Royal Society of Chemistry. (e) Schematic illustration of the fabrication of HsGDY@Cu_2O/CF photocathode. (f) LSV curves of Cu_2O NWs and HsGDY@Cu_2O NWs. Copyright 2022, Springer Nature.

density of 1.74 mA cm^{-2} at 0.6 V *vs.* SCE compared to other photoanodes without NiFe-LDH and rGO.

4.2.3. Graphdiyne. Graphdiyne (GDY), a newly emerging two-dimensional carbon allotrope, consists of both sp- and sp^2-hybridized carbons which are butadiyne linkers and benzene ring moieties, respectively.[123,124] The unique sp-hybridized carbon atoms enable GDY to possess outstanding properties such as abundant carbon bonds, chemical stability, and high electrical conductivity. Zhang *et al.* reported the enhancement of photoelectrochemical properties by inserting GDY nanowall into Si heterojunction (SiHJ)-based photoanode.[125] The GDY wall was coated on SiHJ substrated through a modified Glaser-Hay coupling reaction, then the NiO_x particles were employed by magnetron sputtering. The GDY was synthesized to exhibit high hole mobility of 1×10^4 cm^2 V^{-1} s^{-1} and conductivity of 2.516×10^{-4} S m^{-1} which are well-matched with those of silicon-based substrate. The fabricated SiHJ/GDY/NiO_x photoanode showed an outstanding onset potential of 1.082 V *vs.* RHE and a saturated photocurrent density of 39.1 mA cm^{-2} which is two times higher than that of SiHJ/NiO_x photoanode. The elevated PEC-OER performance is attributed to the excellent conductivity, catalytic activity, and the chemical bonds between GDY and NiO_x inducing synergistic effect. Zhou *et al.* proposed a facile in-situ encapsulation strategy to passivate Cu_2O photocathode and activate water reduction using hydrogen-substituted graphdiyne (HsGDY).[126] As shown in Fig. 7(e), the HsGDY@Cu_2O/CF photocathode was fabricated *via* a three-step process of electrochemical anodization, annealing, and Glaser-coupling. For the Glaser-coupling reaction, 1,3,5-triethynylbenzene (TEB), piperidine, pyridine, and Cu(I) ion were used as precursor, ligand, solvent, and catalyst, respectively. After the reaction, the giant two-dimensional network structure of HsGDY consisting of large organic hexatomic rings, alternating-distributed benzene ring, and alkynyl was formed. In Fig. 7(f), the optimized HsGDY@Cu_2O NWs/CF exhibited a high photocurrent density of −12.88 mA cm^{-2} at 0 V *vs.* RHE, which is much higher than that of pristine Cu_2O NWs/CF.

4.3. Black phosphorus (BP)

Black phosphorus, one of the allotropes of phosphorus, is a thermodynamically stable layered semiconductor having a narrow band gap that can be obtained from white or red phosphorus at high pressure and temperature due to a phase transition.[127] To date, pressure-induced atomic structural change of 2D material has only been identified in black phosphorus as orthorhombic atomic structure changes to rhombohedral and cubic at 5 and 10 GPa, respectively. The high carrier mobility of black phosphorus and tunable energy band gap from 0.3 to 2.0 eV enables them to become a promising material in various electronic and energy conversion applications.

Zheng *et al.* firstly constructed a TiO_{2-x}/BP heterojunction photoanode with the strategies of black phosphorus quantum

dots (BPQDs) sensitization and oxygen vacancies introduction to TiO_2 nanotube arrays (NTAs).[128] The BPQDs were prepared by dispersing BP crystals in NMP and sonicating them for several hours. The BPQDs were spin-coated onto the TiO_2 NTAs in which the oxygen vacancies were created after being soaked in $NaBH_4$ solution. In Fig. 8(a) and (b), TEM images of TiO_{2-x}/BP photoanode were provided and the distinct lattice fringes of 0.270 nm correspond to the (040) planes of BP, indicating that BPQDs have been successfully synthesized. The synergistic effect of the synthesized BPQDs and oxygen vacancies induced NTAs enhances the PEC performance by improving charge separation and increasing active sites. Fig. 8(c) shows the LSV curve of the TiO_{2-x}/BP electrode and it produced a photocurrent density of 1.12 mA cm^{-2} at 1.23 V *vs.* RHE, which is more than three times that of pristine TiO_2.

Zhang *et al.* verified that the intrinsic p-type black phosphorus contributes to the hole extraction from $BiVO_4$ photoanode and prolongs the trapping lifetime of charges on the $BiVO_4$ surface by characterizing OEC/BP/$BiVO_4$.[129] In Fig. 8(d), the density of states (DOS) of BP/$BiVO_4$ heterojunction was provided and it was confirmed that BP nanosheets change the valence band of $BiVO_4$ *via* the overlap of the P 2p and O 2p orbitals without affecting the conduction band minimum of $BiVO_4$. The band offset and built-in potential of the BP/$BiVO_4$ heterojunction are demonstrated in Fig. 8(e). Under external bias, the positrons serving as the dominant carriers across the BP/$BiVO_4$ heterointerface promote hole extraction from $BiVO_4$ to BP. As shown in Fig. 8(f), an obvious increase in photocurrent density derived from the insertion of BP was observed. The NiOOH/BP/$BiVO_4$ photoanode achieved a photocurrent density of 4.48 mA cm^{-2} at 1.23 V *vs.* RHE, which is 1.5 times higher than that of the NiOOH/$BiVO_4$ photoanode. Furthermore, the insertion of BP also improved the charge separation efficiency of $BiVO_4$ as can be seen in Fig. 8(g). The enhanced charge separation efficiency clearly proved the role of BP as an efficient hole extraction material. In addition, the introduction

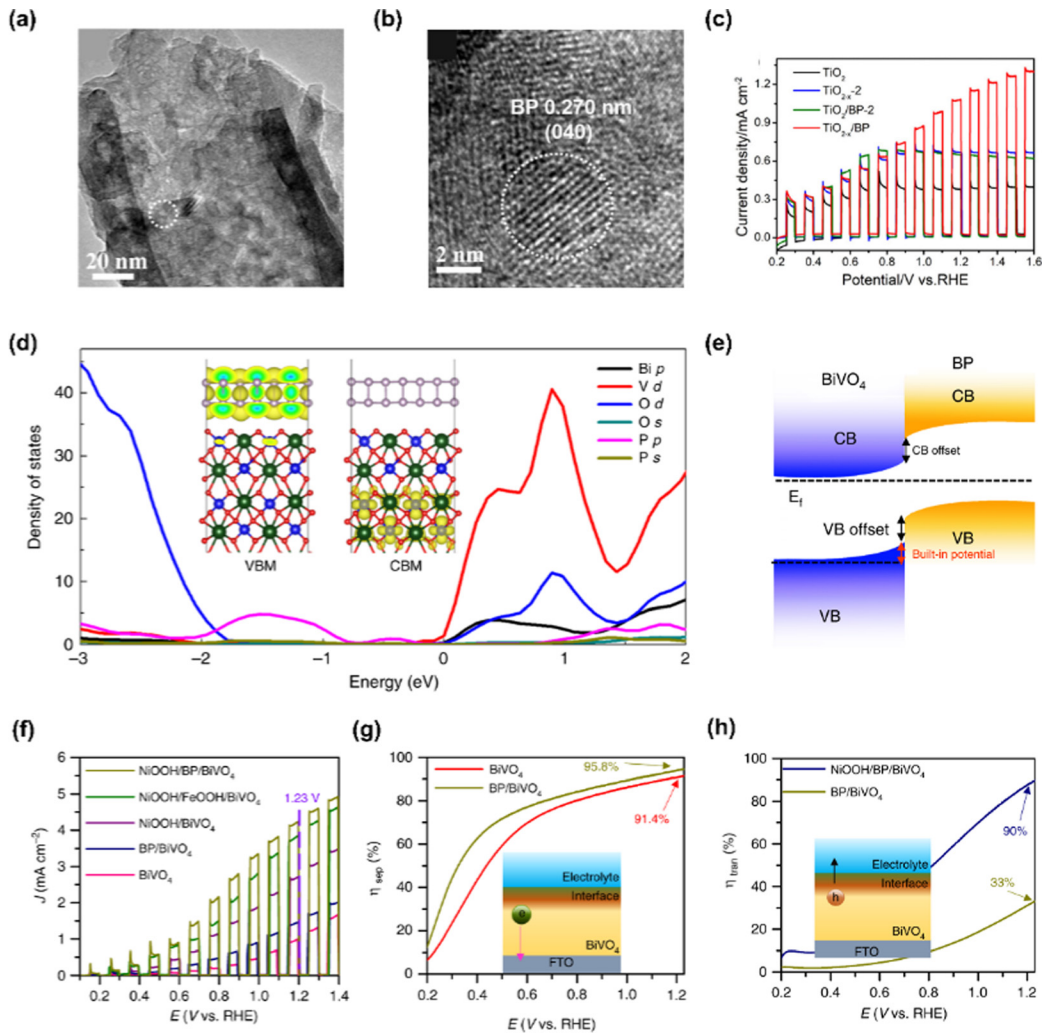

Fig. 8 (a) TEM and (b) HR-TEM images of TiO_{2-x}/BP. (c) LSV curves of TiO_2, TiO_{2-x}-2, TiO_2/BP-2, and TiO_{2-x}/BP. Copyright 2020, American Chemical Society. (d) Density of states (DOS) of BP/$BiVO_4$ heterojunction. (e) Energy band diagram of BP/$BiVO_4$. (f) Chopped LSV curves of $BiVO_4$, BP/$BiVO_4$, NiOOH/$BiVO_4$, NiOOH/FeOOH/$BiVO_4$, and NiOOH/BP/$BiVO_4$. (g) Charge separation efficiencies and (h) charge transfer efficiencies of $BiVO_4$ and BP/$BiVO_4$. Copyright 2019, Springer Nature.

of the NiOOH catalyst on BP/$BiVO_4$ boosted the charge transfer efficiency, enabling highly efficient water oxidation at the surface.

4.4. Layered double hydroxides (LDHs)

LDHs are a type of anionic clay having a layered structure defined as a unique atomic formula of $[M_{1-x}^{2+}M_x^{3+}(OH)_2](A^{n-})_{x/n}\cdot mH_2O$. M^{2+} and M^{3+} are divalent and trivalent metal cations, and A^{n-} is a charge-balancing anion.[130] Mg, Fe, Co, Cu, Ni, Zn are used as M^{2+}, and Al, Cr, Ga, Mn are used as M^{3+}. Commonly, LDHs consist of layers of metal cations having similar ionic radii, which are coordinated by six oxygen atoms with the structure of $M^{2+}/M^{3+}(OH)_6$ octahedra.[131] These octahedra construct two-dimensional sheet by sharing edges and the sheets are stacked together *via* hydrogen bonding between the hydroxyl groups.

Chong *et al.* demonstrated a highly efficient and stable α-Fe_2O_3 photoanode in neutral pH condition by decorating CoAl-LDH *via* the hydrothermal method.[132] In Fig. 9(a), the TEM image shows the successful synthesis of CoAl-LDH and compact integration of LDH with α-Fe_2O_3. In Fig. 9(b), the LSV curves of α-Fe_2O_3, CoAl-LDH/α-Fe_2O_3, Co–OH/α-Fe_2O_3, Al–OH/α-Fe_2O_3, and CoPi/α-Fe_2O_3 were provided. Compared to bare α-Fe_2O_3, the CoAl-LDH/α-Fe_2O_3 exhibited drastically improved PEC water oxidation in neutral pH electrolyte as the onset potential was shifted to cathodic direction by 250 mV and the photocurrent density was increased 9-fold at 1.23 V *vs.* RHE. The authors explained that Co provided active sites for water oxidation while Al provided the support for the layered skeleton. In addition, the layered structure assisted H_2O to access the Co active sites. Not only in neutral pH electrolyte but also in high pH media, CoAl-LDH/α-Fe_2O_3 shows superior PEC-OER performance at various applied potentials as can be seen in Fig. 9(c).

Choi *et al.* fabricated a Si photoanode with remarkable PEC performance using cyclic voltammetry (CV)-activated amorphous TiO_2 and NiFe LDH.[133] Amorphous TiO_2 interlayer was synthesized *via* ALD method followed by CV activation in 1 M NaOH solution with the applied potential from −1 to 1 V *vs.* Ag/AgCl. After this procedure, NiFe LDH thin film catalyst was synthesized by electrodeposition. In Fig. 9(d), the TEM image of NiFe LDH/activated α-TiO_2/n-Si and the HR-TEM image of NiFe LDHs were presented. The hierarchical porous structure of NiFe LDH was compactly formed on α-TiO_2/n-Si substrate and it is beneficial to the smooth release of the product and the diffusion of ions. The PEC-OER performance of the fabricated NiFe LDH/activated 5 nm α-TiO_2/n-Si photoanode is shown in Fig. 9(e). For the photoanode without TiO_2 activation, poor performance was shown due to a large band gap, facile charge recombination, and low charge transfer of the TiO_2 layer. After CV activation of TiO_2, the photoanode showed superior *J–V* characteristics due to oxygen vacancies facilitating hole transfer. The synergistic heterostructure exhibited an onset potential of 0.92 ± 0.1 V *vs.* RHE and a photocurrent density of 36 mA cm^{-2} at 1.23 V *vs.* RHE.

4.5. Graphitic carbon nitride (g-C_3N_4)

Graphitic carbon nitride (g-C_3N_4) is considered an attractive material in photoelectrochemistry and photocatalysis due to its

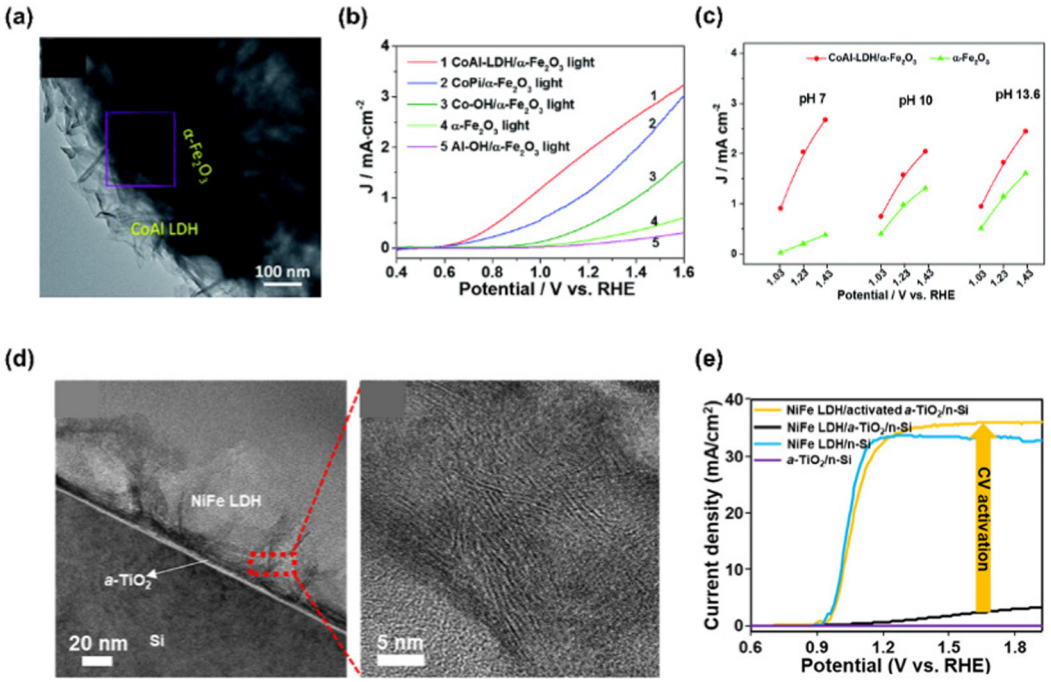

Fig. 9 (a) TEM image of CoAl LDH/α-Fe_2O_3. (b) LSV curves of α-Fe_2O_3, CoAl-LDH/α-Fe_2O_3, Co–OH/α-Fe_2O_3, Al–OH/α-Fe_2O_3 and CoPi/α-Fe_2O_3. (c) Current densities for bare α-Fe_2O_3 and CoAl-LDH/α-Fe_2O_3 at 1.03, 1.23 and 1.43 V *vs.* RHE in electrolytes with different pH values of 7, 10 and 13.6. Copyright 2017, Royal Society of Chemistry. (d) TEM image of NiFe LDHs/activated α-TiO_2/n-Si and HR-TEM image of NiFe LDHs. (e) LSV curves of NiFe LDH/activated α-TiO_2/n-Si, NiFe LDH/α-TiO_2/n-Si, NiFe LDH/n-Si and α-TiO_2/n-Si. Copyright 2020, American Chemical Society.

excellent visible light reactivity, suitable band gap, physicochemical stability, low cost, and pollution-free feature.[134] However, there are some restrictions to be improved such as insufficient solar light absorption, low surface area, and fast charge recombination. To date, various strategies to obtain high-performance g-C_3N_4 have been conducted by elemental doping, morphology control, enlarging porosity, and heterostructuring.[135,136]

Wen *et al.* fabricated an all-solid-state 3D urchin-like ZnO/Au/g-C_3N_4 heterojunction photocathode showing a highly efficient PEC hydrogen evolution.[137] For the fabrication of the photocathode, ZnO seeds were grown into 3D urchin-like ZnO nanorods by hydrothermal method and Au was deposited by ultrasonication of ZnO nanorods with $HAuCl_4$ precursor. Then, g-C_3N_4 was synthesized by thermal vapor condensation (TVC) in melamine III followed by coating on the FTO substrate by drop casting. In Fig. 10(a), the TEM image shows that Au nanoparticles are well attached to urchin-like ZnO and g-C_3N_4 surrounds the Au NPs compactly. The schematic in Fig. 10(b) shows the charge transfer mechanism of ZnO/Au/g-C_3N_4 ternary heterojunction under light illumination. In this mechanism, Au NPs with high work function (−5.30 eV) act as mediators promoting electron transfer from ZnO to g-C_3N_4, facilitating the Z-scheme charge carriers process. The improved performance of the electrode was confirmed in Fig. 10(c), which shows the LSV curves of several photoelectrodes including the ZnO/Au/g-C_3N_4 photoelectrode. ZnO/Au/g-C_3N_4 yields a photocurrent density of −0.91 mA cm^{-2} at −0.4 V *vs.* RHE. In addition, ZnO/Au/g-C_3N_4 showed remarkable stability, producing a value of −0.29 mA cm^{-2} for more than 36 000 s.

Jiang *et al.* demonstrated a vertical 3D printing strategy for an efficient photoelectrode with vertically aligned and hierarchically porous g-C_3N_4/CNT arrays.[138] A printable ink was developed to print g-C_3N_4/CNT arrays and it consisted of g-C_3N_4, CNT, lignin, and Pluronic F-127. Pluronic F-127 was used to adjust the viscosity of the ink. Fig. 10(e) shows that ink is printed on the FTO substrate and the structure of 3D g-C_3N_4/CNTs facilitates electron propagation from g-C_3N_4 to the CNT, thereby promoting hydrogen production capacity. Well-aligned g-C_3N_4/CNTs and disordered g-C_3N_4/CNTs are shown in Fig. 10(f) and (g), respectively. A distinct charge redistribution was observed throughout the well-aligned g-C_3N_4/CNTs surface, whereas in the disordered g-C_3N_4/CNTs, it was only observed at

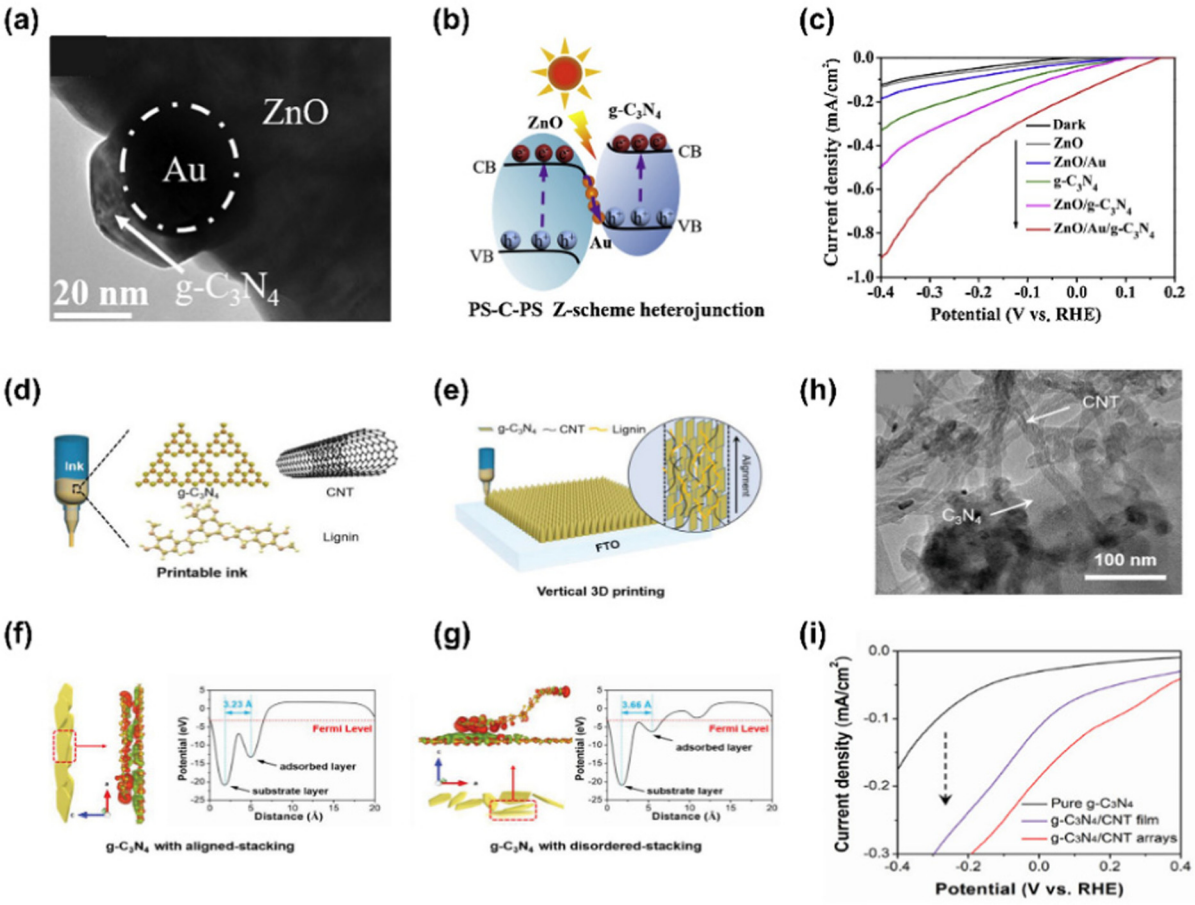

Fig. 10 (a) TEM image of urchin-like ZnO/Au/g-C_3N_4. (b) The charge transfer mechanism of ZnO/Au/g-C_3N_4 ternary heterojunction. (c) LSV curves of ZnO, ZnO/Au, g-C_3N_4, ZnO/g-C_3N_4, and ZnO/Au/g-C_3N_4. Copyright 2020, Elsevier. (d) The schematic of main composition of the printable ink for vertically aligned and hierarchically porous g-C_3N_4/CNT arrays. (e) Vertical 3D printing of g-C_3N_4/CNT/lignin on FTO. (h) TEM image of CNT and g-C_3N_4 showing the tight interaction of ink component. DFT simulations of charge redistributions and plane-averaged electrostatic potential in (f) vertically aligned and (g) disordered g-C_3N_4. (i) LSV curves of g-C_3N_4, g-C_3N_4/CNT film, and g-C_3N_4/CNT arrays. Copyright 2021, Wiley-VCH GmbH.

the ends of the sheets. The average electrostatic potential profile also shows that the well-aligned g-C_3N_4/CNTs (d = 3.23 Å) have a smaller interlayer distance than the disordered ones (d = 3.66 Å). A TEM image in Fig. 10(h) shows that CNTs were uniformly coated on the g-C_3N_4 surface. It was confirmed that the CNTs were entangled and supported each other. The LSV curves in Fig. 10(i) show that the printed arrays produce significantly higher photocurrent density than pure g-C_3N_4 and g-C_3N_4/CNT film.

4.6. MXenes

2D MXenes, composed of transition metal carbides, nitrides, and carbonitrides, are obtained by etching "A" element from ternary "MAX" structure, where "M" is a transition metal such as Ti, Mo, V, "A" is Al or Ga, and "X" is C or N.[139] Recently, MXene has drawn tremendous attention due to great conductivity, large surface area, exposed active metal sites, and excellent dispersibility enabling them to be utilized in various applications.[140–142] Interestingly, the unique 2D MXene analogues such as nitrogen-rich Mo_5N_6 nanosheets and $V_{0.2}Mo_{0.8}N_{1.2}$ solid solution have recently been developed for electrochemical HER.[143–145] Compared with conventional MXenes, they showed significantly enhanced catalytic activity due to their modified electronic state.

Ye *et al.* successfully designed highly active and stable α-Fe_2O_3 NRs by coating 2D Ti_3C_2-MXene using a facile hydrothermal and annealing process.[146] In Fig. 10(a), the fabrication of α-Fe_2O_3/MXene NRs photoanode was shown. Firstly, β-FeOOH/MXene NRs were prepared by hydrothermal method on FTO substrates with a solution of $FeCl_3$, $NaNO_3$, and prepared Ti_3C_2-MXene. After that, the substrate was washed and heat-treated to prepare α-Fe_2O_3/MXene NRs. Fig. 11(b) shows the LSV curves of photoanodes produced with various MXene ratios. α-Fe_2O_3/$MXene_{10/1}$ NRs with a small amount of MXene produced a photocurrent density of 0.60 mA cm^{-2} at 1.23 V *vs.* RHE, which is a four-fold improvement over that of bare hematite NRs. As the atomic ratio of Ti increases, the PEC performance of the photoanode tends to increase, but if the amount of MXene is excessively increased, the growth of nanorods is inhibited, so the PEC performance decreases. As a result, the α-Fe_2O_3/$MXene_{5/1}$ NRs produced the largest photocurrent density with a value of 1.10 mA cm^{-2} at 1.23 V *vs.* RHE.

Yin *et al.* reported an efficient photoanode by depositing $Ti_3C_2T_x$ MXene on Fe-doped TiO_2 nanorod arrays.[147] Fe–TiO_2 nanorod arrays were prepared by hydrothermal method, and MXene was synthesized by electrodeposition. Fig. 11(c) shows $Ti_3C_2T_x$ nanosheets adhered well to Fe–TiO_2 nanorod arrays after electrodeposition. TEM image of MXene in Fig. 11(d) shows 2D $Ti_3C_2T_x$ nanosheets with single or several layers which were well exfoliated with a thickness of less than 2.2 nm. The PEC-OER performance of the as-fabricated Fe–TiO_2/$Ti_3C_2T_x$ photoanode can be confirmed in Fig. 11(e). The Fe–TiO_2/$Ti_3C_2T_x$ photoanode, electrodeposited for 240 seconds, showed the best performance with a photocurrent density of

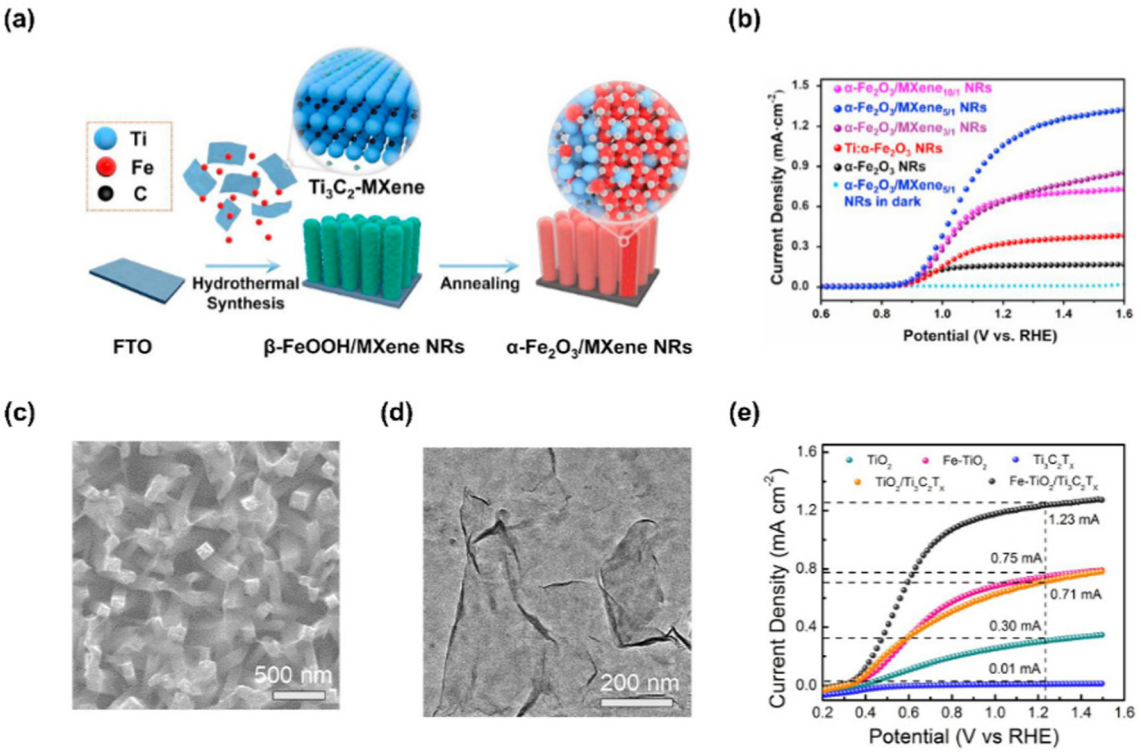

Fig. 11 (a) Schematic of fabrication process for α-Fe_2O_3/$MXene_n$ NRs. (b) LSV curves α-Fe_2O_3, NRs, Ti:α-Fe_2O_3, α-Fe_2O_3/$MXene_{3/1}$ NRs, α-Fe_2O_3/$MXene_{5/1}$ NRs, and α-Fe_2O_3/$NXene_{10/1}$ NRs. Copyright 2021, Elsevier. (c) SEM image of the Fe–TiO_2/$Ti_3C_2T_x$. (d) TEM image of the exfoliated $Ti_3C_2T_x$ nanosheets. (e) LSV curves of TiO_2, $Ti_3C_2T_x$, TiO_2/$Ti_3C_2T_x$, Fe–TiO_2 (Fe: 5 mol%) and Fe–TiO_2/$Ti_3C_2T_x$. Copyright 2022, Elsevier.

1.23 mA cm^{-2} at 1. 23 V *vs.* RHE, which is higher than that of other TiO_2-based photoelectrodes. This result is derived from the superiority of $Ti_3C_2T_x$ nanosheets improving the charge transfer efficiency and water oxidation kinetics of Fe–TiO_2.

5. Conclusion and perspective

Solar energy, one of the unlimited energy sources transferred to the earth, can satisfy our desire to produce hydrogen energy without CO_2 emission. In this respect, it is necessary to develop inexpensive and high-quality photoelectrodes for low-cost hydrogen production. However, photoelectrode itself can not sufficiently boost the surface reaction, accelerate photogenerated charge transfer, and protect the corrosion. Thus, it is essential to investigate highly catalytic, conductive, and robust materials to support the photoelectrodes. In this review, we summarized the superiorities of 2D materials and introduced the utilization of various 2D materials for photoelectrochemical water splitting. The van der Waals interactions between layers allow them to have unique properties such as large specific surface area, stackability for heterostructure, tunable band gap, and surface functionalization. With these distinctions, they not only support but also act as photoelectrodes. Firstly, their catalytic activity improves the surface reaction producing hydrogen and oxygen. In particular, deliberately enlarged active edge sites and defects contribute to lowering free energy to be required for HER and OER, leading to a low overpotential and high photocurrent density. Also, phase transformation, ion-exchanged sites and synergistically mixed composites enable 2D materials to surpass their intrinsic catalytic activity. Secondly, 2D materials serve as interfacial transporting layers *via* energetically favorable Schottky junctions, p–n junctions, and multi-heterojunctions as there is no intrinsic surface state within band gap and they can be stacked into substrates without crystal mismatch and atomic interdiffusion. Thirdly, chemically inert 2D materials protect the surface of silicon and oxide-based photoelectrodes vulnerable to the acidic and alkaline electrolyte. Finally, 2D materials having an energy band gap can absorb solar energy and generate electron–hole pairs. Though they intrinsically provide a small amount of photocurrent density, their photoelectrochemical performance can be enhanced by surface treatments and layer stacking.

Until now, a variety of 2D materials have been revealed and applied to the field of (photo)electrochemistry. We classified them into transition metal dichalcogenides, carbon allotropes, black phosphorus, layered double hydroxides, g-C_3N_4, and MXene. Many researchers have strengthened the potential of 2D materials for practical utilization in PEC applications. Despite significant progress in integrating 2D materials into various semiconducting photoabsorbers, there are still issues that must be addressed for the further improvement of the device. Firstly, it is necessary to directly synthesize 2D materials on photoelectrodes with uniformity and large-scale size for practical industrial application. In some research, TMDs and graphene have grown on SiO_2 wafer and copper foil, respectively, to obtain high-quality layers. Then, they were transferred on top of photoelectrodes. However, it is not applicable to mass production in which highly uniform and large-scale synthesis should be prioritized. Thus, a technology capable of direct synthesis of 2D materials on photoelectrodes must be developed. Secondly, 2D materials do not chemically adhere to substrates but have physisorption with them, causing a fatal problem that easily falls off during the reaction. As a result, the PEC performance of the device dramatically decreases after desorption. To solve this phenomenon, it is essential to develop a new process that can increase adhesion. Finally, research should be proceeded until the stage of constructing a tandem device for unassisted solar water splitting. If the solar-to-hydrogen efficiency is obtained from a tandem device decorated with 2D materials, the value of 2D materials in the practical industry will be more recognized. We believe that our inclusive review regarding 2D materials for photoelectrochemical water splitting could inspire researchers interested in renewable energy, photoelectrochemical catalysts, and 2D materials.

Author contributions

SE Jun and JK Lee contributed equally to this work. They wrote the manuscript under the supervision of HW Jang. All authors contributed to the general discussion.

Conflicts of interest

The authors declare that there are no conflicts of interest.

Acknowledgements

This work was supported by the National Research Foundation of Korea (NRF) grant funded by the Korea government Ministry of Science and ICT (MSIT) (2022M3H4A1A01011963). This research was also supported by the KRISS (Korea Research Institute of Standards and Science) MPI Lab. program. The Inter-University Semiconductor Research Center and Institute of Engineering Research at Seoul National University provided research facilities for this work.

References

1 A. Fujishima and K. Honda, *Nature*, 1972, **238**, 37–38.
2 N. S. Lewis and D. G. Nocera, *Proc. Natl. Acad. Sci. U. S. A.*, 2006, **103**, 15729–15735.
3 J. Gong, C. Li and M. R. Wasielewski, *Chem. Soc. Rev.*, 2019, **48**, 1862–1864.
4 J. Graetz, *Chem. Soc. Rev.*, 2009, **38**, 73–82.
5 A. Züttel, *Mater. Today*, 2003, **6**, 24–33.
6 P. Chen and M. Zhu, *Mater. Today*, 2008, **11**, 36–43.
7 J. J. Alves and G. P. Towler, *Ind. Eng. Chem. Res.*, 2002, **41**, 5759–5769.

8 N. Armaroli and V. Balzani, *ChemSusChem*, 2011, **4**, 21–36.
9 J. O. Abe, A. Popoola, E. Ajenifuja and O. Popoola, *Int. J. Hydrogen*, 2019, **44**, 15072–15086.
10 H. Park, I. J. Park, M. G. Lee, K. C. Kwon, S.-P. Hong, D. H. Kim, S. A. Lee, T. H. Lee, C. Kim and C. W. Moon, *ACS Appl. Mater. Interfaces*, 2019, **11**, 33835–33843.
11 H. Park, J. W. Bae, T. H. Lee, I. J. Park, C. Kim, M. G. Lee, S. A. Lee, J. W. Yang, M. J. Choi and S. H. Hong, *Small*, 2022, **18**, 2105611.
12 I. Roger, M. A. Shipman and M. D. Symes, *Nat. Rev. Chem.*, 2017, **1**, 1–13.
13 J. H. Kim, D. Hansora, P. Sharma, J.-W. Jang and J. S. Lee, *Chem. Soc. Rev.*, 2019, **48**, 1908–1971.
14 M. R. Shaner, H. A. Atwater, N. S. Lewis and E. W. McFarland, *Energy Environ. Sci.*, 2016, **9**, 2354–2371.
15 M. G. Walter, E. L. Warren, J. R. McKone, S. W. Boettcher, Q. Mi, E. A. Santori and N. S. Lewis, *Chem. Rev.*, 2010, **110**, 6446–6473.
16 G. Zeng, T. A. Pham, S. Vanka, G. Liu, C. Song, J. K. Cooper, Z. Mi, T. Ogitsu and F. M. Toma, *Nat. Mater.*, 2021, **20**, 1130–1135.
17 L. Pan, J. H. Kim, M. T. Mayer, M.-K. Son, A. Ummadisingu, J. S. Lee, A. Hagfeldt, J. Luo and M. Grätzel, *Nat. Catal.*, 2018, **1**, 412–420.
18 W. Yang, J. H. Kim, O. S. Hutter, L. J. Phillips, J. Tan, J. Park, H. Lee, J. D. Major, J. S. Lee and J. Moon, *Nat. Commun.*, 2020, **11**, 1–10.
19 B. Koo, D. Kim, P. Boonmongkolras, S. R. Pae, S. Byun, J. Kim, J. H. Lee, D. H. Kim, S. Kim and B. T. Ahn, *ACS Appl. Energy Mater.*, 2020, **3**, 2296–2303.
20 S. A. Lee, T. H. Lee, C. Kim, M. G. Lee, M.-J. Choi, H. Park, S. Choi, J. Oh and H. W. Jang, *ACS Catal.*, 2018, **8**, 7261–7269.
21 S. A. Lee, T. H. Lee, C. Kim, M.-J. Choi, H. Park, S. Choi, J. Lee, J. Oh, S. Y. Kim and H. W. Jang, *ACS Catal.*, 2019, **10**, 420–429.
22 M. J. Kenney, M. Gong, Y. Li, J. Z. Wu, J. Feng, M. Lanza and H. Dai, *Science*, 2013, **342**, 836–840.
23 X. Yu, P. Yang, S. Chen, M. Zhang and G. Shi, *Adv. Energy Mater.*, 2017, **7**, 1601805.
24 J. Park, T. H. Lee, C. Kim, S. A. Lee, M.-J. Choi, H. Kim, J. W. Yang, J. Lim and H. W. Jang, *Appl. Catal., B*, 2021, **295**, 120276.
25 J. Park, S. Lee, T. H. Lee, C. Kim, S. E. Jun, J. H. Baek, J. Y. Kim, S. H. Ahn and H. W. Jang, *Nano Convergence*, 2022, **9**, 1–14.
26 M. G. Lee, J. W. Yang, H. Park, C. W. Moon, D. M. Andoshe, J. Park, C.-K. Moon, T. H. Lee, K. S. Choi and W. S. Cheon, *Nano-Micro Lett.*, 2022, **14**, 1–15.
27 M.-J. Choi, T. L. Kim, K. S. Choi, W. Sohn, T. H. Lee, S. A. Lee, H. Park, S. Y. Jeong, J. W. Yang and S. Lee, *ACS Appl. Mater. Interfaces*, 2022, **14**, 7788–7795.
28 J. W. Yang, I. J. Park, S. A. Lee, M. G. Lee, T. H. Lee, H. Park, C. Kim, J. Park, J. Moon and J. Y. Kim, *Appl. Catal., B*, 2021, **293**, 120217.
29 S. S. Bhat, J. M. Suh, S. Choi, S.-P. Hong, S. A. Lee, C. Kim, C. W. Moon, M. G. Lee and H. W. Jang, *J. Mater. Chem. A*, 2018, **6**, 14633–14643.
30 Y. Zhao, K. R. Yang, Z. Wang, X. Yan, S. Cao, Y. Ye, Q. Dong, X. Zhang, J. E. Thorne and L. Jin, *Proc. Natl. Acad. Sci. U. S. A.*, 2018, **115**, 2902–2907.
31 S. A. Lee, J. W. Yang, T. H. Lee, I. J. Park, C. Kim, S. H. Hong, H. Lee, S. Choi, J. Moon and S. Y. Kim, *Appl. Catal., B*, 2022, 121765.
32 Z. Luo, T. Wang and J. Gong, *Chem. Soc. Rev.*, 2019, **48**, 2158–2181.
33 W. Yang, R. R. Prabhakar, J. Tan, S. D. Tilley and J. Moon, *Chem. Soc. Rev.*, 2019, **48**, 4979–5015.
34 D. Bae, B. Seger, P. C. Vesborg, O. Hansen and I. Chorkendorff, *Chem. Soc. Rev.*, 2017, **46**, 1933–1954.
35 S. A. Lee, S. Choi, C. Kim, J. W. Yang, S. Y. Kim and H. W. Jang, *ACS Mater. Lett.*, 2019, **2**, 107–126.
36 E. Zhao, K. Du, P. F. Yin, J. Ran, J. Mao, T. Ling and S. Z. Qiao, *Adv. Sci.*, 2022, **9**, 2104363.
37 C. Li, Q. Cao, F. Wang, Y. Xiao, Y. Li, J.-J. Delaunay and H. Zhu, *Chem. Soc. Rev.*, 2018, **47**, 4981–5037.
38 H. R. Kwon, H. Park, S. E. Jun, S. Choi and H. W. Jang, *Chem. Commun.*, 2022, **58**, 7874–7889.
39 Y. Zhu, J. Ren, X. Yang, G. Chang, Y. Bu, G. Wei, W. Han and D. Yang, *J. Mater. Chem. A*, 2017, **5**, 9952–9959.
40 H. Chen, S. Wang, J. Wu, X. Zhang, J. Zhang, M. Lyu, B. Luo, G. Qian and L. Wang, *J. Mater. Chem. A*, 2020, **8**, 13231–13240.
41 C.-J. Chen, V. Veeramani, Y.-H. Wu, A. Jena, L.-C. Yin, H. Chang, S.-F. Hu and R.-S. Liu, *Appl. Catal., B*, 2020, **263**, 118259.
42 K. C. Kwon, S. Choi, K. Hong, C. W. Moon, Y.-S. Shim, T. Kim, W. Sohn, J.-M. Jeon, C.-H. Lee and K. T. Nam, *Energy Environ. Sci.*, 2016, **9**, 2240–2248.
43 X. Chia and M. Pumera, *Nat. Catal.*, 2018, **1**, 909–921.
44 A. K. Geim and I. V. Grigorieva, *Nature*, 2013, **499**, 419–425.
45 H. Long, A. Harley-Trochimczyk, T. Pham, Z. Tang, T. Shi, A. Zettl, C. Carraro, M. A. Worsley and R. Maboudian, *Adv. Funct. Mater.*, 2016, **26**, 5158–5165.
46 A. Chaves, J. G. Azadani, H. Alsalman, D. Da Costa, R. Frisenda, A. Chaves, S. H. Song, Y. D. Kim, D. He, J. Zhou, A. Castellanos-Gomez, F. Peeters, Z. Liu, C. Hinkle, S.-H. Oh, P. D. Ye, S. J. Koester, Y. H. Lee, P. Avouris, X. Wang and T. Low, *npj 2D Mater. Appl.*, 2020, **4**, 1–21.
47 N. Martín, N. Tagmatarchis, Q. H. Wang and X. Zhang, *Chem. – Eur. J.*, 2020, **26**, 6292–6295.
48 Z. Sun, T. Ma, H. Tao, Q. Fan and B. Han, *Chem*, 2017, **3**, 560–587.
49 J. Mao, T. Zhou, Y. Zheng, H. Gao, H. K. Liu and Z. Guo, *J. Mater. Chem. A*, 2018, **6**, 3284–3303.
50 T. H. Eom, S. H. Cho, J. M. Suh, T. Kim, T. H. Lee, S. E. Jun, J. W. Yang, J. Lee, S.-H. Hong and H. W. Jang, *J. Mater. Chem. A*, 2021, **9**, 11168–11178.
51 Z. Li, Z. Zhuang, F. Lv, H. Zhu, L. Zhou, M. Luo, J. Zhu, Z. Lang, S. Feng, W. Chen, L. Mai and S. Guo, *Adv. Mater.*, 2018, **30**, 1803220.
52 A. R. Fareza, F. A. A. Nugroho, F. F. Abdi and V. Fauzia, *J. Mater. Chem. A*, 2022, **10**, 8656–8686.

53 S. S. M. Bhat, S. A. Pawar, D. Potphode, C.-K. Moon, J. M. Suh, C. Kim, S. Choi, D. S. Patil, J.-J. Kim, J. C. Shin and H. W. Jang, *Appl. Catal., B*, 2019, **259**, 118102.
54 S. A. Lee, J. W. Yang, S. Choi and H. W. Jang, *Exploration*, 2021, **1**, 20210012.
55 M. Long, P. Wang, H. Fang and W. Hu, *Adv. Funct. Mater.*, 2019, **29**, 1803807.
56 S. Y. Park, Y. H. Kim, S. Y. Lee, W. Sohn, J. E. Lee, D. H. Kim, Y.-S. Shim, K. C. Kwon, K. S. Choi, H. J. Yoo, J. M. Suh, M. Ko, J.-H. Lee, M. J. Lee, S. Y. Kim, M. H. Lee and H. W. Jang, *J. Mater. Chem. A*, 2018, **6**, 5016–5024.
57 Y. Wang, J. Pang, Q. Cheng, L. Han, Y. Li, X. Meng, B. Ibarlucea, H. Zhao, F. Yang, H. Liu, H. Liu, W. Zhou, X. Wang, M. H. Rummeli, Y. Zhang and G. Cuniberti, *Nano-Micro Lett.*, 2021, **13**, 143.
58 A. M. Smith and S. Nie, *Acc. Chem. Res.*, 2010, **43**, 190–200.
59 C. Zhang, H. Huang, X. Ni, Y. Zhou, L. Kang, W. Jiang, H. Chen, J. Zhong and F. Liu, *Nanoscale*, 2018, **10**, 16759–16764.
60 A. Ramasubramaniam, D. Naveh and E. Towe, *Nano Lett.*, 2011, **11**, 1070–1075.
61 S. Manzeli, A. Allain, A. Ghadimi and A. Kis, *Nano Lett.*, 2015, **15**, 5330–5335.
62 J. Wan, S. D. Lacey, J. Dai, W. Bao, M. S. Fuhrer and L. Hu, *Chem. Soc. Rev.*, 2016, **45**, 6742–6765.
63 Y. Gong, Z. Liu, A. R. Lupini, G. Shi, J. Lin, S. Najmaei, Z. Lin, A. L. Elías, A. Berkdemir, G. You, H. Terrones, M. Terrones, R. Vajtai, S. T. Pantelides, S. J. Pennycook, J. Lou, W. Zhou and P. M. Ajayan, *Nano Lett.*, 2014, **14**, 442–449.
64 Y. Chen, J. Xi, D. O. Dumcenco, Z. Liu, K. Suenaga, D. Wang, Z. Shuai, Y.-S. Huang and L. Xie, *ACS Nano*, 2013, **7**, 4610–4616.
65 G. Gui, J. Li and J. Zhong, *Phys. Rev. B: Condens. Matter Mater. Phys.*, 2008, **78**, 075435.
66 Z. H. Ni, T. Yu, Y. H. Lu, Y. Y. Wang, Y. P. Feng and Z. X. Shen, *ACS Nano*, 2008, **2**, 2301–2305.
67 Z. Wang, P. Liu, Y. Ito, S. Ning, Y. Tan, T. Fujita, A. Hirata and M. Chen, *Sci. Rep.*, 2016, **6**, 1–9.
68 L. Daukiya, J. Seibel and S. De Feyter, *Adv. Phys.: X*, 2019, **4**, 1625723.
69 S. Presolski and M. Pumera, *Mater. Today*, 2016, **19**, 140–145.
70 A. R. Brill, E. Koren and G. de Ruiter, *J. Mater. Chem. C*, 2021, **9**, 11569–11587.
71 C. Liu, C. Kong, F.-J. Zhang, C.-M. Kai, W.-Q. Cai, X.-Y. Sun and W.-C. Oh, *J. Korean Ceram. Soc.*, 2021, **58**, 135–147.
72 M. G. Lee, J. W. Yang, H. R. Kwon and H. W. Jang, *CrystEngComm*, 2022, **24**, 5838–5864.
73 B. You, M. T. Tang, C. Tsai, F. Abild-Pedersen, X. Zheng and H. Li, *Adv. Mater.*, 2019, **31**, 1807001.
74 J. Huang, H. Gao, Y. Xia, Y. Sun, J. Xiong, Y. Li, S. Cong, J. Guo, S. Du and G. Zou, *Nano Energy*, 2018, **46**, 305–313.
75 J. Zhang, X. Xu, L. Yang, D. Cheng and D. Cao, *Small Methods*, 2019, **3**, 1900653.
76 H. Li, C. Tsai, A. L. Koh, L. Cai, A. W. Contryman, A. H. Fragapane, J. Zhao, H. S. Han, H. C. Manoharan, A.-P. Frank and J. K. Nørskov, *Nat. Mater.*, 2016, **15**, 48–53.
77 C. Tsai, H. Li, S. Park, J. Park, H. S. Han, J. K. Nørskov, X. Zheng and F. Abild-Pedersen, *Nat. Commun.*, 2017, **8**, 1–8.
78 T. F. Jaramillo, K. P. Jørgensen, J. Bonde, J. H. Nielsen, S. Horch and I. Chorkendorff, *Science*, 2007, **317**, 100–102.
79 R. Fan, J. Mao, Z. Yin, J. Jie, W. Dong, L. Fang, F. Zheng and M. Shen, *ACS Appl. Mater. Interfaces*, 2017, **9**, 6123–6129.
80 S. E. Jun, S. P. Hong, S. Choi, C. Kim, S. G. Ji, I. J. Park, S. A. Lee, J. W. Yang, T. H. Lee, W. Sohn, J. Y. Kim and H. W. Jang, *Small*, 2021, **17**, 2103457.
81 J. W. Hill, Z. Fu, J. Tian and C. M. Hill, *J. Phys. Chem. C*, 2020, **124**, 17141–17149.
82 W. Huang, Q. Zhou, S. Su, J. Li, X. Lu, X. Gao, X. Wang, M. Jin, G. Zhou, Z. Zhang and J. Liu, *Adv. Mater. Interfaces*, 2019, **6**, 1801663.
83 D. Voiry, A. Mohite and M. Chhowalla, *Chem. Soc. Rev.*, 2015, **44**, 2702–2712.
84 Z. Lei, J. Zhan, L. Tang, Y. Zhang and Y. Wang, *Adv. Energy Mater.*, 2018, **8**, 1703482.
85 F. Xiong, H. Wang, X. Liu, J. Sun, M. Brongersma, E. Pop and Y. Cui, *Nano Lett.*, 2015, **15**, 6777–6784.
86 X. Wang, X. Shen, Z. Wang, R. Yu and L. Chen, *ACS Nano*, 2014, **8**, 11394–11400.
87 Z. Lai, Y. Yao, S. Li, L. Ma, Q. Zhang, Y. Ge, W. Zhai, B. Chi, B. Chen, L. Li, L. Wang, Z. Zheng, L. Gu, Y. Du and H. Zhang, *Adv. Mater.*, 2022, 2201194.
88 Q. Ding, F. Meng, C. R. English, M. Cabán-Acevedo, M. J. Shearer, D. Liang, A. S. Daniel, R. J. Hamers and S. Jin, *J. Am. Chem. Soc.*, 2014, **136**, 8504–8507.
89 K. C. Kwon, S. Choi, J. Lee, K. Hong, W. Sohn, D. M. Andoshe, K. S. Choi, Y. Kim, S. Han, S. Y. Kim and H. W. Jang, *J. Mater. Chem. A*, 2017, **5**, 15534–15542.
90 S. Choi, C. Kim, J. Y. Lee, T. H. Lee, K. C. Kwon, S. Kang, S. A. Lee, K. S. Choi, J. M. Suh, K. Hong, S. E. Jun, W. K. Kim, S. H. Ahn, S. Han, S. Y. Kim, C.-H. Lee and H. W. Jang, *Chem. Eng. J.*, 2021, **418**, 129369.
91 J. E. Thorne, Y. Zhao, D. He, S. Fan, S. Vanka, Z. Mi and D. Wang, *Phys. Chem. Chem. Phys.*, 2017, **19**, 29653–29659.
92 G. Yang, S. Li, X. Wang, B. Ding, Y. Li, H. Lin, D. Tang, X. Ren, Q. Wang, S. Luo and J. Ye, *Appl. Catal., B*, 2021, **297**, 120268.
93 C. K. Ku, P. H. Wu, C. C. Chung, C. C. Chen, K. J. Tsai, H. M. Chen, Y. C. Chang, C. H. Chuang, C. Y. Wei, C. Y. Wen, T.-Y. Lin, H.-L. Chen, Y.-S. Wang, Z.-Y. Lee, J.-R. Chang, C.-W. Luo, D.-Y. Wang, B. J. HWang and C.-W. Chen, *Adv. Energy Mater.*, 2019, **9**, 1901022.
94 K. C. Kwon, S. Choi, K. Hong, C. W. Moon, Y.-S. Shim, T. Kim, W. Sohn, J.-M. Jeon, C.-H. Lee, K. T. Nam, S. Han, S. Y. Kim and H. W. Jang, *Energy Environ. Sci.*, 2016, **9**, 2240–2248.
95 D. Ghosh, P. Devi and P. Kumar, *ACS Appl. Mater. Interfaces*, 2020, **12**, 13797–13804.
96 S. Seo, S. Kim, H. Choi, J. Lee, H. Yoon, G. Piao, J. C. Park, Y. Jung, J. Song, S. Y. Jeong, H. Park and S. Lee, *Adv. Sci.*, 2019, **6**, 1900301.

97 S. E. Jun, S. Choi, S. Choi, T. H. Lee, C. Kim, J. W. Yang, W.-O. Choe, I.-H. Im, C.-J. Kim and H. W. Jang, *Nano-Micro Lett.*, 2021, **13**, 1–16.
98 U. Sim, T.-Y. Yang, J. Moon, J. An, J. Hwang, J.-H. Seo, J. Lee, K. Y. Kim, J. Lee, S. Han, B. H. Hong and K. T. Nam, *Energy Environ. Sci.*, 2013, **6**, 3658–3664.
99 L. A. King, T. R. Hellstern, J. Park, R. Sinclair and T. F. Jaramillo, *ACS Appl. Mater. Interfaces*, 2017, **9**, 36792–36798.
100 X. Yu, N. Guijarro, M. Johnson and K. Sivula, *Nano Lett.*, 2018, **18**, 215–222.
101 L. Wang, M. Tahir, H. Chen and J. B. Sambur, *Nano Lett.*, 2019, **19**, 9084–9094.
102 B. Zhou, X. Kong, S. Vanka, S. Chu, P. Ghamari, Y. Wang, N. Pant, I. Shih, H. Guo and Z. Mi, *Nat. Commun.*, 2018, **9**, 1–8.
103 K. C. Kwon, S. Choi, K. Hong, D. M. Andoshe, J. M. Suh, C. Kim, K. S. Choi, J. H. Oh, S. Y. Kim and H. W. Jang, *MRS Commun.*, 2017, **7**, 272–279.
104 P. Gnanasekar, D. Periyanagounder, P. Varadhan, J.-H. He and J. Kulandaivel, *ACS Appl. Mater. Interfaces*, 2019, **11**, 44179–44185.
105 C.-C. Chung, H. Yeh, P.-H. Wu, C.-C. Lin, C.-S. Li, T.-T. Yeh, Y. Chou, C.-Y. Wei, C.-Y. Wen and Y.-C. Chou, *ACS Nano*, 2021, **15**, 4627–4635.
106 W. Huang, Q. Zhou, S. Su, J. Li, X. Lu, X. Gao, X. Wang, M. Jin, G. Zhou and Z. Zhang, *Adv. Mater. Interfaces*, 2019, **6**, 1801663.
107 D. M. Andoshe, G. Jin, C. S. Lee, C. Kim, K. C. Kwon, S. Choi, W. Sohn, C. W. Moon, S. H. Lee and J. M. Suh, *Adv. Sustainable Syst.*, 2018, **2**, 1700142.
108 A. Hasani, Q. Van Le, M. Tekalgne, M.-J. Choi, S. Choi, T. H. Lee, H. Kim, S. H. Ahn, H. W. Jang and S. Y. Kim, *ACS Appl. Mater. Interfaces*, 2019, **11**, 29910–29916.
109 Y. Liu, J. Wu, K. P. Hackenberg, J. Zhang, Y. M. Wang, Y. Yang, K. Keyshar, J. Gu, T. Ogitsu and R. Vajtai, *Nat. Energy*, 2017, **2**, 1–7.
110 K. S. Novoselov, A. K. Geim, S. V. Morozov, D.-E. Jiang, Y. Zhang, S. V. Dubonos, I. V. Grigorieva and A. A. Firsov, *Science*, 2004, **306**, 666–669.
111 Y. Zhang, Y.-W. Tan, H. L. Stormer and P. Kim, *Nature*, 2005, **438**, 201–204.
112 A. A. Balandin, *Nat. Mater.*, 2011, **10**, 569–581.
113 R. R. Nair, P. Blake, A. N. Grigorenko, K. S. Novoselov, T. J. Booth, T. Stauber, N. M. Peres and A. K. Geim, *Science*, 2008, **320**, 1308.
114 X. Du, I. Skachko, A. Barker and E. Y. Andrei, *Nat. Nanotechnol.*, 2008, **3**, 491–495.
115 C. Lee, X. Wei, J. W. Kysar and J. Hone, *Science*, 2008, **321**, 385–388.
116 X. Li, J. Yu, S. Wageh, A. A. Al-Ghamdi and J. Xie, *Small*, 2016, **12**, 6640–6696.
117 U. Sim, J. Moon, J. An, J. H. Kang, S. E. Jerng, J. Moon, S.-P. Cho, B. H. Hong and K. T. Nam, *Energy Environ. Sci.*, 2015, **8**, 1329–1338.
118 F.-X. Xiao, J. Miao and B. Liu, *J. Am. Chem. Soc.*, 2014, **136**, 1559–1569.
119 K.-Y. Yoon, J.-S. Lee, K. Kim, C. H. Bak, S.-I. Kim, J.-B. Kim and J.-H. Jang, *ACS Appl. Mater. Interfaces*, 2014, **6**, 22634–22639.
120 S. Chandrasekaran, J. S. Chung, E. J. Kim and S. H. Hur, *Chem. Eng. J.*, 2016, **290**, 465–476.
121 U. Sim, J. Moon, J. Lee, J. An, H.-Y. Ahn, D. J. Kim, I. Jo, C. Jeon, S. Han and B. H. Hong, *ACS Appl. Mater. Interfaces*, 2017, **9**, 3570–3580.
122 F. Ning, M. Shao, S. Xu, Y. Fu, R. Zhang, M. Wei, D. G. Evans and X. Duan, *Energy Environ. Sci.*, 2016, **9**, 2633–2643.
123 X. Gao, H. Liu, D. Wang and J. Zhang, *Chem. Soc. Rev.*, 2019, **48**, 908–936.
124 H. Yu, Y. Xue and Y. Li, *Adv. Mater.*, 2019, **31**, 1803101.
125 S. Zhang, C. Yin, Z. Kang, P. Wu, J. Wu, Z. Zhang, Q. Liao, J. Zhang and Y. Zhang, *ACS Appl. Mater. Interfaces*, 2018, **11**, 2745–2749.
126 X. Zhou, B. Fu, L. Li, Z. Tian, X. Xu, Z. Wu, J. Yang and Z. Zhang, *Nat. Commun.*, 2022, **13**, 1–10.
127 H. Liu, Y. Du, Y. Deng and D. Y. Peide, *Chem. Soc. Rev.*, 2015, **44**, 2732–2743.
128 L. Zheng, X. Ye, X. Deng, Y. Wang, Y. Zhao, X. Shi and H. Zheng, *ACS Sustainable Chem. Eng.*, 2020, **8**, 15906–15914.
129 K. Zhang, B. Jin, C. Park, Y. Cho, X. Song, X. Shi, S. Zhang, W. Kim, H. Zeng and J. H. Park, *Nat. Commun.*, 2019, **10**, 1–10.
130 J. Han, Y. Dou, J. Zhao, M. Wei, D. G. Evans and X. Duan, *Small*, 2013, **9**, 98–106.
131 A. I. Khan and D. O'Hare, *J. Mater. Chem.*, 2002, **12**, 3191–3198.
132 R. Chong, B. Wang, C. Su, D. Li, L. Mao, Z. Chang and L. Zhang, *J. Mater. Chem. A*, 2017, **5**, 8583–8590.
133 S. Choi, S. A. Lee, H. Yang, T. H. Lee, C. Kim, C. W. Lee, H. Shin and H. W. Jang, *ACS Appl. Energy Mater.*, 2020, **3**, 12298–12307.
134 L. Jiang, X. Yuan, Y. Pan, J. Liang, G. Zeng, Z. Wu and H. Wang, *Appl. Catal., B*, 2017, **217**, 388–406.
135 Y. Li, R. Wang, H. Li, X. Wei, J. Feng, K. Liu, Y. Dang and A. Zhou, *J. Phys. Chem. C*, 2015, **119**, 20283–20292.
136 S. S. Bhat, S. E. Jun, S. A. Lee, T. H. Lee and H. W. Jang, *Energies*, 2020, **13**, 974.
137 P. Wen, Y. Sun, H. Li, Z. Liang, H. Wu, J. Zhang, H. Zeng, S. M. Geyer and L. Jiang, *Appl. Catal., B*, 2020, **263**, 118180.
138 B. Jiang, H. Huang, W. Gong, X. Gu, T. Liu, J. Zhang, W. Qin, H. Chen, Y. Jin and Z. Liang, *Adv. Funct. Mater.*, 2021, **31**, 2105045.
139 M. Naguib, M. Kurtoglu, V. Presser, J. Lu, J. Niu, M. Heon, L. Hultman, Y. Gogotsi and M. W. Barsoum, *Adv. Mater.*, 2011, **23**, 4248–4253.
140 H. Huang, J. Cui, G. Liu, R. Bi and L. Zhang, *ACS Nano*, 2019, **13**, 3448–3456.
141 X. Fan, Y. Ding, Y. Liu, J. Liang and Y. Chen, *ACS Nano*, 2019, **13**, 8124–8134.
142 H.-S. Lim, S. B. Choi, H. Kwon, J.-W. Lim, C. J. Han, J.-M. Oh and J.-W. Kim, *Electron. Mater. Lett.*, 2021, **17**, 513–520.
143 H. Jin, H. Yu, H. Li, K. Davey, T. Song, U. Paik and S. Z. Qiao, *Angew. Chem., Int. Ed.*, 2022, e202203850.

144 H. Jin, X. Liu, A. Vasileff, Y. Jiao, Y. Zhao, Y. Zheng and S.-Z. Qiao, *ACS Nano*, 2018, **12**, 12761–12769.
145 H. Jin, T. Song, U. Paik and S.-Z. Qiao, *Acc. Mater. Res.*, 2021, **2**, 559–573.
146 R.-K. Ye, S.-S. Sun, L.-Q. He, S.-R. Yang, X.-Q. Liu, P.-P. Fang and J.-Q. Hu, *Appl. Catal., B*, 2021, **291**, 120107.
147 H. Yin, Y. Wang, L. Ma, S. Zhang, B. Yang and R. Jiang, *Chem. Eng. J.*, 2022, **431**, 134124.